# NUMERICAL ANALYSIS OF THE INTERACTION BETWEEN A DETONATION WAVE AND COMPRESSIBLE HOMOGENEOUS ISOTROPIC TURBULENCE

by

MONIKA CHAUHAN

Presented to the Faculty of the Graduate School of
The University of Texas at Arlington in Partial Fulfillment
of the Requirements
for the Degree of

MASTER OF SCIENCE IN MECHANICAL ENGINEERING

THE UNIVERSITY OF TEXAS AT ARLINGTON

May 2011

To my parents, loving sisters and fiancé

who motivated me in this excellent research.

ACKNOWLEDGEMENTS

I would like to express my deep gratitude to my research advisors — Dr. Frank Lu and Dr. Luca Massa — for providing me a great opportunity to carry out this invaluable research work. I am thankful to them for granting me financial support for pursuing my Master of Science studies. Dr. Lu has supervised me with consistent motivation and encouragement and has been a great mentor throughout my research work. I would like to thank Dr. Massa for his vital role in sharing his insight and excellent knowledge in Fortran, Matlab programming, etc., and for his availability which helped a lot in getting me over my research. I would like to thank Dr. Donald R. Wilson for consenting to be on my committee and for taking the time to read, evaluate and give a critical review of this thesis.

I would like to thank all the staff in the Mechanical and Aerospace Engineering Department and the Texas Advanced Computing Center, Austin, Texas, for their support and help in my research and Master's studies. I include a special thanks to Dr. Albert Tong, for financial aid and his advisement. Thanks also go to Mr. Makoto Sadahiro of TACC who helped in using TACC resources for scientific visualization.

Finally, I would like to thank those who are dear to me — my family, fiancé and friends. Sincere gratitude goes to my brother-in-law who has inspired and encouraged me in critical thinking for my research. Thanks to my sisters in the United States and family back in India who supported me spiritually and encouraged me all through my studies. I also would like to thank Sushil Rai, my fiancé, for his patience, support and help during my stay in United States. Thanks to my goddess Durga for her blessings.

April 18, 2011

ABSTRACT

NUMERICAL ANALYSIS OF THE INTERACTION BETWEEN A DETONATION WAVE AND COMPRESSIBLE HOMOGENEOUS ISOTROPIC TURBULENCE

Monika Chauhan, M.S.

The University of Texas at Arlington, 2011

Supervising Professors: Dr. Luca Massa and Dr. Frank Lu

A numerical study was performed to investigate the effect of preshock turbulence on detonation wave properties. A direct numerical simulation was performed on the chemically reactive Navier–Stokes equations using a Runge–Kutta scheme and a fifth-order WENO spatial discretization. A simple one-step chemical kinetics model was used in the study.

The main objective of the research is to examine the behavior of the turbulence when subjected to a strong shock with heat release. The evolution of the turbulent Mach number, lengthscales (Taylor microscale and Kolmogorov scale), turbulent kinetic energy, Reynolds stress, auto-correlations with heat release and activation energy is examined. Shock–turbulence interaction have been the subject of research for over the decades but there is no significant study that has yet been made on Detonation–Turbulence interaction. This research is helpful in practical applications such as safe handling of the fuels, promoting detonations for detonation engines etc..

The results show a marked influence of preshock perturbations on the postshock statistics. Detonation–Turbulence interaction resulted in higher amplifications of turbulence statistics and parameters like turbulent Mach number, turbulent length scales (i.e. Taylor microscale, Kolmogorov length scale etc.), turbulent kinetic energy, velocity fluctuations, auto-correlations etc. The detonation event triggers a self-excited instability, evidenced by the velocity fluctuations and further by space-time correlation functions. Also, the alteration to the limit cycle structure supported by unstable waves close to their critical points is highlighted. The effect of reactivity and fluid acceleration in the postshock region are examined by comparison with the non-reactive analog. The possibility that significant forcing can lead to hot-spot formation is investigated by considering temperature probability distribution functions in the reaction zone. The separate effect of vortical and entropic fluctuations is considered.

TABLE OF CONTENTS

LIST OF FIGURES

LIST OF TABLES

# CHAPTER 1

# INTRODUCTION

The interaction of a detonation wave and homogeneous isotropic turbulence is concerned with the unsteady coupling between the convected turbulence structures and a detonation wave. The dynamics of the interaction is expected to reveal the role of the turbulent field on detonation stability, the occurrence of spinning and galloping detonations, and how the rapid heat release affects the turbulence. The preshock turbulent field is compressible, isotropic and chemically homogeneous whereas the postshock field is strongly nonhomogeneous due to the rapid axial straining and the nonlinear interaction between turbulence and heat release. In general, the interaction between turbulence and heat release affects many combustion processes. In particular, detonation structures interact with a turbulized preshock field both during the initiation [6] and the propagation phases [16] of flame acceleration to detonation. There are various sources where turbulence ahead of the detonation wave can occur, such as in turbulent boundary layers [26], ridges in obstacle laden pipes [10], shock–flame interactions [24], and detonation waves in continuous spin detonation engines [5].

Fundamental understanding of shock–turbulence interaction remains limited, despite decades of efforts. To gain insight, the interaction of a normal shock wave propagating past an isotropic turbulent field has been studied. Basing on shock–turbulence interaction, the present study extends into the problem to detonation–turbulence interaction. Detonation–turbulence interaction differs from shock–turbulence interaction in many ways, but the basic difference between the two is the role of the

chemical induction region in the amplification of convected turbulence in the form of vortical structures. The detonation–turbulence interaction process differs from the non-reactive shock–turbulence analog because of three reasons: exothermicity, the presence of a length scale associated with detonation, and the presence of natural (intrinsic) fluctuations of the unstable detonation front.

Direct numerical simulation was used to solve for the detonation–turbulence interaction. In this simulation, a single-step irreversible Arrhenius chemical reaction was used for simplicity. The present work studies the reactivity effects of preshock turbulence on the integral length scales, Taylor microscales, one-dimensional energy spectra, variances, probability density functions, etc., in the postshock region. The complex interaction requires that the dynamics of the small fluid-mechanics scales and the detonation scales be properly captured. For solving the chemically reactive compressible Navier–Stokes equations for a perfect gas, we have used the Runge–Kutta scheme with fifth-order WENO (weighted essentially non-oscillatory) spatial discretization for shock capturing and for computing the turbulence away from the shock. This method is implemented using parallelized Fortran codes run on several machines housed at TACC (Texas Advanced Computing Center) located in Austin, Texas.

# CHAPTER 2

# DESCRIPTION AND HISTORY BACKGROUND

## 2.1 Brief Description of Detonation – Turbulence Interaction

Detonation–turbulence interaction is a complex phenomenon which is investigated in the present work using direct numerical simulation. Examples where such an interaction may occur include detonation waves interacting with a turbulent boundary layer resulting from the gas dilatation in closed pipes, ridges in obstacle laden pipes, shock–flame interactions and in continuous spin detonation engines. Understanding of this phenomenon is beneficial in different industries, such as the safe handling of fuels and in promoting detonations for detonation engines.

Not much has yet been done in studying detonation–turbulence interaction due to its complexity. Lately, studies were carried out using linear interaction analysis (LIA). Direct numerical simulation [36] was conducted using the WENO scheme with an approximate Riemann solver with a third-order Runge–Kutta scheme for time discretization. A numerical study [34] was performed where the effect of the preshock turbulence on the detonation wave properties was investigated. This study showed that there is a marked influence of the preshock perturbations on the postshock statistics. The significance of forcing, either vortical or entropic, was also investigated. The study showed that hot spots form due to the nonuniform temperature field.

The interaction of the detonation wave with a convected field of a weak turbulence was studied in detail by Ribner et al. [19] where the effect of chemical release on the rms fluctuations downstream of the detonation was examined as a function of Mach number. The greatest changes occur around the Chapman–Jouguet Mach

number due to the effect of exothermicity. Ribner et al. concluded that the one-dimensional power spectrum displays the Kolmogorov decay and is unaffected by the exothermicity. This conclusion was based on the assumption that the reaction zone thickness is much smaller than the turbulence length scales while in actuality the induction zones can be quite large. Recently, a numerical study was performed in which receptivity analysis, energy spectra, probability distribution functions, etc., for the reactive and non-reactive analog are compared [33].

## 2.2 Detonation

A detonation wave is one of a class of propagating combustion waves, the other being deflagration. Essentially, a detonation wave is a shock wave, that is, a supersonic wave that is sustained by the chemical energy released following shock compression. In short, detonation is a supersonic flow phenomena comprising a shock front followed by a reaction. In detonation, two modes of initiation exist: a slow mode known as thermal initiation in where there is a transition from deflagration, and a fast mode which is brought by an ignition blast or strong shock wave. Detonation is obtained by a sequence of events like the development of turbulence in the mixture, compression of combustion waves which leads to shocks and later to a detonation.

A one-dimensional theory for detonations was first formulated by Chapman and Jouguet. The Chapman–Jouguet (CJ) theory states that the solution from integrating the conservation equations is obtained only by assuming the detonation wave as steady, planar and one-dimensional [13], despite the fact that detonation front is multi-dimensional. Chapman and Jouguet established the conditions that the flow behind the supersonic detonation is locally sonic. The point on the reactive hugoniot is the tangent from the initial state and is known as the upper CJ point. A lower CJ point also tangent to the reactive hugoniot is the complementary CJ deflagration

point. It can be noted that despite the success of the CJ theory in modeling detonation, the theory does not account for the time required for the combustion process. Subsequently, Zel'dovich, von Neumann and Döring separately proposed a more realistic one-dimensional model where the planar shock is followed by a reaction zone, initiated after an induction delay [17].

Experimental observations of detonation wave propagation in a tube have shown that when steady-state detonation structures are fully established, the flow structure and the energy release at the wave front are periodic at one mode frequency which is inversely proportional to a cell length. Two-dimensional simulations [14] revealed the dynamics of the cellular detonation front including triple points, transverse waves and unreacted pockets in detail. In unstable detonations, cellular structures are supported by the periodic collision of decaying transverse waves. Other experimental observations found that for large tube diameters, a limiting size is reached for the detonation cell size [13]. Hence, the solid walls play a marginal role in determining the cell size, and computations with periodic boundary conditions can be used to predict the width of patterns recorded on soot foils. In the present work, detonation structures interact with a turbulent preshock field during the propagation phase [16].

Dou et al. [11] performed a numerical, three-dimensional study of the influence of transverse waves on the heat release zone and on the pattern of quasi-steady detonation fronts. They determined that the triple points generated by the motion of transverse waves causes the detonation front to become locally over-driven and form "hot spots" where chemical reaction is enhanced by the coupling of high pressure and high velocity flow. Austin [2] linked the disruption of the regular, periodic, limit cycle structure, and the formation of hot spots in unstable detonations to the mixture effective activation energy.

Detonation is unexplored mainly in the area of detonation instability due to its complexity. In our research, we have studied the detonation wave and turbulence interaction to comprehend this instability, spinning and galloping detonations.

## 2.3 Compressible Homogeneous Isotropic Turbulence And Previous Research

Turbulence has often been called the last unsolved problem of classical physics. There are many fascinating theoretical issues while the importance of turbulence in many applications and in nature ranging from engineering to geophysics and astrophysics is evident. Turbulence has been systematically examined numerically, experimentally and computationally for more than a century. A number of important insights in the understanding of turbulence is still elusive such as the lack of fully satisfactory theories of such basic aspects as transition and the Kolmogorov $k^{-5/3}$ spectrum . One example of the intractability of turbulence is the seemingly easy problem of predicting the evolution of freely decaying, homogeneous turbulence. Freely decaying turbulence means that it is free from mean shear or any body force which might maintain and shape the turbulence [8]. The decay of freely evolving two-dimensional isotropic turbulence was studied by Lowe [30] who discussed Batchelors classical theory which states that the kinetic energy is the only invariant of the flow that predicts the integral scale growth and showed that periodic boundary conditions impose mirror image, long-range correlations of velocity and vorticity. Also, Lowe concluded that these correlations have the potential to influence the dynamical behavior of the turbulence as well.

The main difference between compressible and incompressible turbulent fluctuations, is that in incompressible flows, the full solution is contained solely in the velocity field because the pressure is nothing but an enslaved Lagrange multiplier. In compressible turbulence, the above statement is no longer valid because pressure is

now an autonomous variable and at least one additional physical variable is required for describing the solution.

For the present study, the extra complication arises in the compressibility where the pressure and likewise the density are coupled with the velocity terms. A full solution of the Navier–Stokes equations is sufficient to resolve the turbulence if an adequate fine mesh resolution and proper time increments are used. These would require extremely large computations which can be done through direct numerical simulation (DNS). DNS does not resort to any turbulence model to compute the turbulence length scales.

Rogallo [43] extended DNS methods used for isotropic turbulence to homogeneous turbulence in an incompressible fluid. He compared results against linear theory and experiment for shear, strain, irrotational strain, rotation effects of mean shear and relaxation toward isotropy following axisymmetric strain, which also helped in evaluating several turbulence models. His results and corresponding conclusions set the standard for DNS of homogeneous turbulence. It is important to capture the whole range of spatial and temporal scales of the turbulence where spatial scales can be resolved using the computational mesh from the smallest dissipative scales to the integral scale associated with the motions containing the kinetic energy [38]. Jamme et al. [20] investigated the complete description of turbulence behavior across the shock and the influence of the incoming turbulence on the interaction. They computed the fluctuating vorticity variances and showed that the baroclinic torque is responsible for the production of transverse vorticity. In the vorticity entropy case, there is a greater reduction in the transverse Taylor microscale and the integral scale compared to the longitudinal Taylor microscale where no significant changes occur. DNS of the interaction of a Mach 1.5 shock wave with a turbulent shear flow showed that the sign and magnitude of the correlation between the velocity and the temper-

ature fluctuations have a crucial influence on the kinetic energy amplifications across the shock. Crespo et al.[7] observed that the magnitude during the interaction of the velocity cross-correlation $u'v'$ is decreased.

## 2.4 Previous Research on Shock–Turbulence Interaction

The non-reactive analog, shock–turbulence interaction, has been the subject of several theoretical [19, 15], numerical [28, 20, 12, 40] and experimental [1, 49] investigations. A large portion of past numerical work was done while comparing the inviscid linear interaction analysis (LIA) with nonlinear Navier–Stokes computations. Lee et al. [28] analyzed the nonreactive coupling and found that nonlinear computations agree well with LIA theory [42]. While linear analysis provides useful estimates of the amplification of vorticity fluctuations across the shock, it misses the strong nonlinear dynamics of the energized and highly anisotropic vorticity downstream of the front. Numerical simulation results presented by Rawat and Zhong [40] indicated that transverse vorticity fluctuations are significantly enhanced across the shock and amplifications increased with the increasing Mach number. Taylor microscales were seen to be reduced just behind the shock after which streamwise microscales rapidly evolve. For turbulent Mach number of approximately 0.1, the nonlinear amplification factor for transverse microscales agrees well with the LIA results.

Jackson's analysis [19] of detonation–turbulence interaction was inadequate to provide the detonation lengthscale associated with the heat release which was later considered in [32]. The latter study found that there is a strong dependency of the transfer functions on the perturbation wave number through the ratio between fluctuation wavelength and reaction half length. This phenomenon is absent in shock–turbulence interactions. Although linear analysis provides useful insights, it fails to correctly represent the system dynamics near natural frequencies. LIA [35] of the

reactive case was done by assuming that the reaction zone thickness is much smaller than the turbulence lengthscale. Jackson et. al. therefore, neglected both the effect of detonation structure and of intrinsic scales. They concluded that exothermicity affects the interaction of convected isotropic weak turbulence by amplifying the rms fluctuations downstream of the detonation. The significant effect of exothermicity on the Mach number has been noticed; specifically the greatest changes happen around the CJ condition. Turbulent kinetic energy and spanwise vorticity fluctuations persistently amplified upon the passage through a shock wave and that the spanwise Taylor microscale persistently diminished while considering the highly compressible turbulence in the shock–turbulence interaction [18].

# CHAPTER 3

# GOVERNING EQUATIONS AND NON-DIMENSIONAL FORM

## 3.1 Governing Equations

### 3.1.1 Navier–Stokes Equations

The compressible fluid motion is described by the governing equations which are non-dimensional conservative form of the continuity, momentum and energy equations in Cartesian coordinates. Therefore, the time-dependent, three-dimensional equations in Cartesian form that describes the conservation of mass, momentum, and total energy of a fluid are given by

$$\frac{\partial \rho}{\partial t} + \frac{\partial}{\partial x_j}(\rho u_j) = 0 \tag{3.1}$$

$$\frac{\partial}{\partial t}(\rho u_i) + \frac{\partial}{\partial x_j}(\rho u_i u_j + p\delta_{ij} - \sigma_{ij}) = 0, \quad i = 1, 2, 3 \tag{3.2}$$

$$\frac{\partial E_t}{\partial t} + \frac{\partial}{\partial x_j}(E_t u_j + u_j p + q_j - u_i \sigma_{ij}) = 0 \tag{3.3}$$

where $\rho$ is the density, $p$ is the thermodynamic pressure, $u_i$ is the velocity component in the $i$th direction, $x_j$ and $t$ are the independent variables denoting three-dimensional Cartesian coordinates and time respectively and $\delta_{ij}$ is the Kronecker delta which is given by

$$\delta_{ij} = \begin{cases} 0 & \text{if } i \neq j \\ 1 & \text{if } i = j \end{cases}$$

The viscous stress tensor $\sigma$ for a Newtonian fluid and heat flux vector $q$ are given by

$$\sigma = \frac{\mu}{Re}\left(\nabla\vec{u} + \nabla\vec{u}^T - \frac{2}{3}I_{3,3}\nabla\cdot\vec{u}\right) \tag{3.4}$$

$$\vec{q} = -\frac{\gamma}{\gamma-1}\frac{\mu}{RePr}\nabla T, \tag{3.5}$$

where $I_{3,3}$ is the $3 \times 3$ identity matrix. The dynamic viscosity used in the above equations is given by the simple power-law relation

$$\mu/\mu_g = \left(\frac{T}{T_0}\right)^{0.7}. \tag{3.6}$$

### 3.1.2 The Euler Equations

The Euler equations are the conservation equations neglecting the transport terms found in the Navier–Stokes equations above, namely,

$$\frac{\partial\rho}{\partial t} + \frac{\partial}{\partial x_j}(\rho u_j) = 0 \tag{3.7}$$

$$\frac{\partial}{\partial t}(\rho u_i) + \frac{\partial}{\partial x_j}(\rho u_i u_j + p\delta_{ij}) = 0, \quad i = 1,2,3 \tag{3.8}$$

$$\frac{\partial E_t}{\partial t} + \frac{\partial}{\partial x_j}(E_t u_j + u_j p) = 0 \tag{3.9}$$

An Euler code was used to verify and validate different cases and techniques with the subsequent Navier–Stokes equations.

## 3.2 Single-Step Chemistry

The important characteristics of the propagation of detonation waves can be sufficiently described by a simple, single-step chemistry model. In the single-step mecha-

nism between two perfect gases X and Y, reaction rate $r(T)$ is given by the Arrhenius law which shows the dependence on temperature $T$ through the relation

$$r(T) = K_0 \exp\left(-\frac{\tilde{E}}{T}\right) \tag{3.10}$$

where $K_0$ is the pre-exponential factor which is also known as the rate constant that sets the temporal scale of the reaction and $\tilde{E}$ is the non-dimensional activation energy. The fluid is assumed to be a perfect gas, that is,

$$p^* = \rho R T^* \tag{3.11}$$

where $R$ is the specific gas constant, $p^*$, $R$ and $T^*$ are non-dimensional parameters.

After implementing the single-step chemistry, the governing equations in conservative form can now be written as

$$\frac{\partial \rho}{\partial t} + \frac{\partial}{\partial x_j}(\rho u_j) = 0 \tag{3.12}$$

$$\frac{\partial}{\partial t}(\rho u_i) + \frac{\partial}{\partial x_j}(\rho u_i u_j + p\delta_{ij} - \sigma_{ij}) = 0, \quad i = 1, 2, 3 \tag{3.13}$$

$$\frac{\partial E_t}{\partial t} + \frac{\partial}{\partial x_j}(E_t u_j + u_j p + q_j - u_i \sigma_{ij}) = 0 \tag{3.14}$$

$$\frac{\partial \rho\lambda}{\partial t} + \frac{\partial}{\partial x_j}(\rho\lambda u_j + \rho J_j) = (\rho - \rho\lambda) r(T), \tag{3.15}$$

The mass diffusion velocity $\vec{J}$ in equation (3.15) is given by

$$\vec{J} = -\frac{\nu}{RePrLe}\nabla\lambda \tag{3.16}$$

where $\nu = \mu/\rho$ is the kinematic viscosity.

The variable $\lambda$ is the reaction progress, where $\lambda = 0$ and 1 are the unburnt state and the completely burnt state respectively. The total energy of the fluid is defined as the sum of the internal energy and the kinetic energy and is given by

$$E_t = \frac{P}{\gamma - 1} + \rho \left( \frac{u_i^2}{2} - \tilde{Q}\lambda \right) \tag{3.17}$$

where $\tilde{Q}$ is the non-dimensional heat release so that the term $\tilde{Q}\rho\lambda$ denotes the non-dimensional chemical energy released as heat during the burning process.

The single-step mechanism for detonation waves was validated by Oran et al. [23] by simulations of flame acceleration and deflagration-to-detonation transition in a large obstructed channel filled with a stoichiometric methane–air mixture. Experimental data were used to qualitatively compare the simulation results. Moreover, single-step kinetics has been employed in many numerical studies for simplicity and for capturing the main effects of chemical nonequilibrium without being bogged down by computational complexities. The effect of this simplified chemistry on the detonation–turbulence interaction is mainly on the coupling between the fluid mechanics scales (i.e, convective, turbulent and eigenvalue)and the chemical scales represented by the eigenvalues of the source term Jacobian.

## 3.3 Non-Dimensional Form Of Equations

The non-dimensional form is needed to independently vary the characteristic parameters, namely, the Mach number $M$, the Reynolds number $Re$ and the Prandtl number $Pr$. Taylor microscales of the flow upstream of the shock are used for non-dimensionalization except for cases where there is no incoming turbulence, namely the unforced cases. Simulation of the incoming homogeneous isotropic turbulence is carried out temporal simulation in a periodic box where initial flow variables are

the random velocity fluctuations with the prescribed spectra. Velocity fluctuations, temperature and upstream fluid density $\rho^*$ are selected to non-dimensionalize all the flow variables and functions. The nondimensional parameters are:

$$x_i^* = \frac{x_i}{L}, \qquad t^* = \frac{t}{\frac{L}{V_\infty}}, \qquad \mu^* = \frac{\mu}{\mu_\infty}, \qquad \rho^* = \frac{\rho}{\rho_\infty}, \tag{3.18}$$

$$T^* = \frac{T}{T_\infty}, \qquad e^* = \frac{e}{V_\infty^2}, \qquad u_i^* = \frac{u_i}{V_\infty}, \qquad p^* = \frac{p}{\rho_\infty V_\infty^2} \tag{3.19}$$

For the reactive terms, the non-dimensionalized parameters are given by

$$Q^* = \frac{Q_{\rho_\infty}}{P_\infty}, \qquad E^* = \frac{E_{\rho_\infty}}{P_\infty}, \qquad K_0^* = K_0 \frac{L}{V_\infty} \tag{3.20}$$

In the above equations, the non-dimensionalized parameters are denoted by $*$ and freestream conditions are denoted by $\infty$.

The free stream Mach number $M_\infty$ and the Reynolds number $Re$ are given by

$$M_\infty = \frac{V_\infty}{\sqrt{\gamma R T_\infty}} \tag{3.21}$$

$$Re_L = \frac{\rho_\infty V_\infty L}{\nu} \tag{3.22}$$

where $L$ is is selected by taking the wave length of the first overtone equal to the Taylor microscale before the temporal decay, i.e. $L = 2\pi\lambda_{TD}$. Since, temporal decay decreases the microscale by a factor of approximately 0.68, so that in non-dimensional units $L = 2\pi\lambda_{TD}/\lambda_0 \approx 9.2$.

# CHAPTER 4

# COMPUTATIONAL SET UP AND BOUNDARY CONDITIONS

## 4.1 Schematic of Computational Flow Set-up

To study the interaction of a detonation wave with compressible homogeneous isotropic turbulence, a schematic of computational flow is created as shown below in Fig. 4.1. The governing equations are solved in a three-dimensional domain size with a square transverse section $(y - z)$ and periodic boundary conditions at the $x - y$ and $x - z$ planes. The computational structure is uniform in the transverse directions but is non-uniform in the streamwise direction, so that points are clustered in the vicinity of the shock.

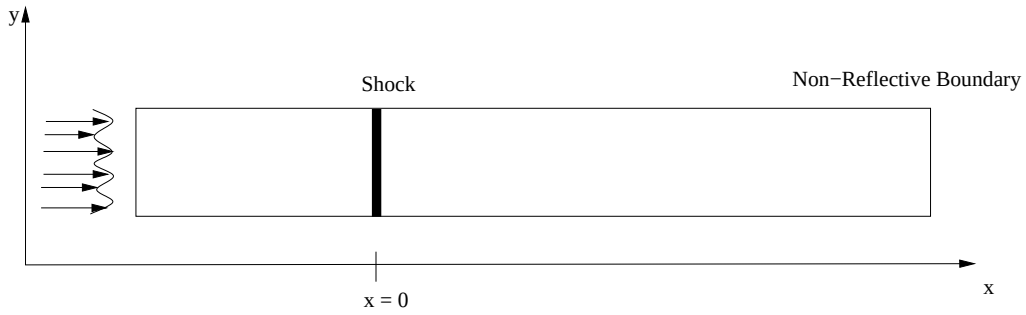


Figure 4.1. Computational set-up.

### 4.1.1 Computational Grid

All computations are performed on a $500 \times 101 \times 101$ grid with stretching mapping in the $x$-direction where the transformation from the computational to the physical space $\xi \rightarrow x$ is assigned in a piecewise polynomial form $x = \mathcal{P}(\xi)$ of order $p$. This analytical transformation is designed to cluster points around the shock wave. The computational domain extends to $\xi \in [\xi_1 \xi_2]$, the shock is at $\xi_0 = 0$, and the mapping has the property that $\mathcal{P}(\xi_i) = \xi_i, \quad i = 0,\ 1,\ 2$. The upper limit $\xi_2 > 0$ corresponds with the shock location where the progress of reaction becomes larger than $1 \times 10^{-8}$, while the fixed value $\xi_1 = -3$ is considered for the lower limit. The analysis is mainly focused on the postshock conditions. Therefore, the grid is maintained uniform and fine immediately after the shock by assigning

$$\mathcal{P}(\xi_1) = \xi_1, \quad \mathcal{P}(\xi_2) = \xi_2 \tag{4.1}$$

$$\frac{d\mathcal{P}}{d\xi}(\xi_1) = 3, \quad \frac{d\mathcal{P}}{d\xi}(\xi_2) = 2 \tag{4.2}$$

$$\frac{d\mathcal{P}}{d\xi}(\xi_0) = 0.1, \quad \frac{d\mathcal{P}}{d\xi^k}(\xi_0) = 0,\ k = 2, \ldots, 5. \tag{4.3}$$

The transformed computational mapping is shown in Fig. 4.2. The domain which

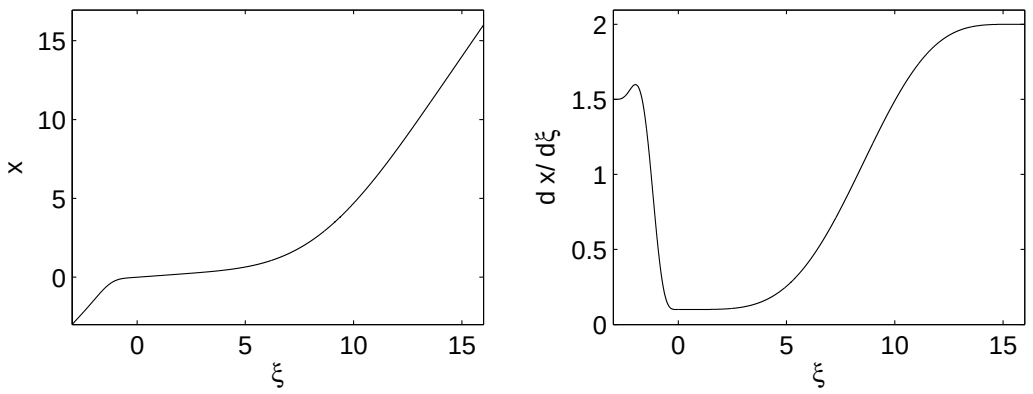


Figure 4.2. Computational mapping stretched along the streamwise direction.

is extended in the direction perpendicular to the mean shock front is $L_y = L_z = L = 9.1961$ where $L$ is selected by taking the wavelength of the first overtone equal to the Taylor microscale before the temporal decay, that is, $L = 2\pi\lambda_{TD}$. Temporal decay decreases the microscale by a factor of approximately 0.68, so that in non-dimensional units $L = 2\pi\lambda_{TD}/\lambda_0 \approx 9.2$.

### 4.1.2 Grid Resolution

DNS of isotropic turbulence requires that the viscous dissipation be fully resolved. Larsson and Lele [25] mentioned severe grid requirements for the simulation of shock–turbulence interaction when using high-order WENO methods. Hence, for $Re_\lambda = 40$, they suggested $153 \times 10^6$ allocation points. It has been observed that the streamwise and transverse vorticity components change differently at the shock after considering the approximate scaling of the Kolmogorov length scale. A decrease in the Kolmogorov scale is also observed. This change is quite obvious due to the compressive nature of the shock and it has an effect on the necessary grid resolution. Hence, resolution for the postshock viscous dissipation requires at least 2.5 times as many grid points as needed for resolving the preshock dissipation in every direction.

DNS of detonation–turbulence interaction is more tractable that shock - turbulence interaction from the standpoint of grid resolution because the large increase in postshock temperature leads to an increase in the viscosity coefficient proportionally as given by equation(3.6). Also, due to heat release, the larger postshock Mach number weakens the coupling between the dilatation-dominated region near the shock and the vorticity-dominated region further the downstream. There is no upstream propagation of disturbance because of the limit of unit overdrive and also become the flow is supersonic. Therefore, only downstream dissipation of vorticity scales has a weak effect on the region near shock.

For the low heat release case [33], grid resolution for the three-dimensional viscous problem was carried out with vortical inflow forcing. The coarse grid was stretched for $500 \times 101 \times 101$ configuration; the fine grid was $500 \times 151 \times 151$ with the same stretching having approximately double the total number of collocation points as the coarse one. Both coarse and fine grids featured 125 points in the reaction half length due to the mapping. All results for density, longitudinal and transverse velocity, and temperature variances [33]are shown in Fig. 4.3. The figure shows a good level of convergence of velocity, density and the temperature variances against the grid size for the problem. Therefore, after this analysis, the stretched $500 \times 101 \times 101$ grid with component-wise WENO-LF reconstruction was selected as a proper candidate for the three-dimensional viscous analysis discussed in next chapter.

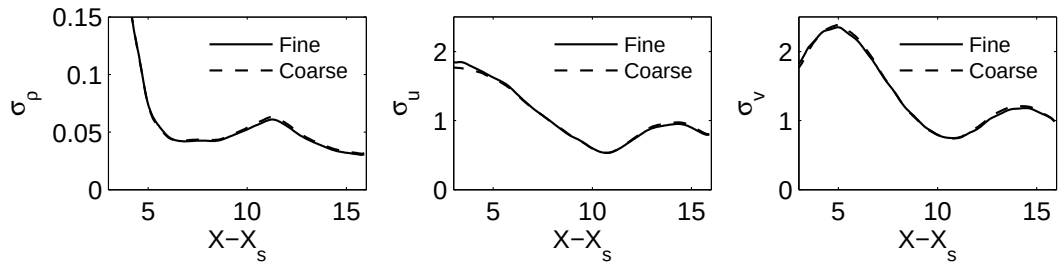


Figure 4.3. Convergence of velocity, density and the temperature variances against the grid size.

## 4.2 Implementation Of Boundary Conditions

Nonreflective boundary conditions are implemented at the subsonic outflow boundary while supersonic inflow conditions are implemented at the inflow boundary.

### 4.2.1 Inflow Boundary Conditions

The conditions at the inflow [33, 28, 31, 27] are implemented by imposing the fluid state on the supersonic inflow side. The turbulent velocity field upstream of the shock wave is isotropic, and the mean flow is uniform. The shock wave is stationary in the mean. Turbulence immediately upstream of the shock is realizable, fully-developed and well characterized. All flow variables are specified at the inflow boundary only. The coordinate system ($x$, $y$, $z$) is such that mean stream is aligned in the longitudinal direction. The incoming flow is assumed to consist of a "frozen" turbulent field which is convected by the mean across the inflow boundary. Turbulent fluctuations are superposed onto the mean field at the inflow boundary where these turbulent fluctuations are obtained from the single realization of a separate temporal simulation of decaying turbulence as mentioned below in the procedure. Temporal simulation is advanced in time until the flow field is developed.

Since the inflow "turbulence" is artificial, the flow takes some distance to evolve into a realistic turbulent flow. Hence, the computational domain upstream of the shock is taken as sufficiently long so that turbulence interacting with the shock wave is taken as a realistic flow with the velocity derivative skewness that would range between $-0.4$ and $-0.5$. Essentially, the flow is decomposed into a mean and a perturbation part where the perturbation is evaluated by the temporal decay of homogeneous isotropic compressible turbulence in a cuboidal set up with periodic boundary conditions. The behavior of the initial spectrum is Gaussian and symmetric with the kinetic energy density given by

$$\varepsilon(k) = \frac{16\sqrt{\frac{2}{\pi}}\exp\left(-\frac{2k^2}{k_0^2}k^4\right)}{k_0^5}, \tag{4.4}$$

where $k_0$ is the wavenumber of the maximum kinetic energy density whose value is equal to $6\pi/L$, where $L$ is the size of the periodic computational box; that is, $k_0$ is three times the wavenumber of the first overtone ($L = 2\pi\lambda_{TD}$). The numerical algorithm used in the present investigation was validated by comparing the isotropic turbulence decay against experimental and computational literature [36]. This study also demonstrated a good match with the measurements obtained with $k_0 = 6\pi/L$.

The temporal decay simulation is started with a solenoidal velocity field $\triangle\ u = 0$, zero pressure and density fluctuations, a turbulent Mach number $M_t = 0.235$, and a fluctuation Reynolds number $Re_\lambda \equiv \rho_0 u_{rms}\lambda/\mu_0 = 100$. The temporal evolution is stopped when the velocity derivative skewness $S_u \equiv \overline{(\partial u_1/\partial x_1)^3}/\overline{(\partial u_1/\partial x_1)^2}^{3/2}$ stabilizes close to the value of $-0.5$ [31]. Spatial realization is used to model the inflow boundary conditions corresponding to the $t = 3$ solution, for which the inflow turbulent Mach number $M_t = 0.235$. Time-decayed turbulence is rescaled so that the length and velocity scales are the Taylor micro-scale $\lambda$ and the velocity rms respectively.

### 4.2.2 Outflow Boundary Conditions

Non-reflecting boundary conditions are implemented at the subsonic outflow boundary conditions. The flow behind the shock is subsonic; therefore, it is necessary to ensure that the flow does not generate acoustic reflections from the outflow boundary conditions. A sponge layer is used in the boundary conditions in the streamwise direction to suppress wave reflections.

## 4.3 Scales

The following scales are used in detonation–turbulence interaction: the rms of the longitudinal velocity at the inflow $u_{rms,0}$, the inflow Taylor microscale $\lambda_0$ based

Table 4.1. Input parameters for the simulations

| Parameter | | |
|---|---|---|
| Grid Size | $N$ | $500 \times 101 \times 101$ |
| Reynolds Number based on the Taylor microscale | $Re$ | 100 |
| Kinematic viscosity | $\mu$ | 0.1 |
| Turbulent Mach number | $M$ | 0.235 |
| Specific heat ratio | $\gamma$ | 1.2 |
| Prandtl Number | $Pr$ | 0.7 |
| Lewis Number | $Le$ | 1 |
| Overdrive | $f$ | 1 |
| Max allowable Courant number | CFL | 0.9 |
| Desired Courant number | CFL | 0.3 |
| Freestream Mach number (low heat release) | $M$ | 4 |
| Freestream Mach number (high heat release) | $M$ | 5.5 |
| Nondimensional low heat release | $Q$ | 19.18 |
| Nondimensional high heat release | $Q$ | 38.57 |
| Activation energy for low heat release | $E$ | 12 |
| Activation energy for high heat release | $E$ | 20 |

on the dissipation function, the preshock unperturbed density $\rho_0$, and the specific gas constant $R$. For the case where there is no incoming turbulence, called the non-forced or natural detonation case, the above choice of scales is maintained. In linear analysis of detonation instability [35], the growth rate eigenvalue and associated eigenfunctions are reported with a slightly different choice of scales. Here, the reaction half length $L_{1/2}$ and the preshock pressure $p_0$ were used instead of $\lambda_0$ and $u_{rms,0}$. The reaction half length is defined as the distance from the lead shock to where the one-dimensional ZND solution reaches a progress of reaction equal to one half. Table 4.1 summarizes the all of the required parameters used for the simulation for the different cases.

# CHAPTER 5

# NUMERICAL ALGORITHM

## 5.1 Numerical Algorithm

The compressible, reactive Navier–Stokes equations for a perfect gas with specific heat ratio of $\gamma = 1.2$ are solved using a numerical algorithm that is third-order in time and fifth-order in space. A fifth-order accurate WENO (weighted essentially non-oscillatory) scheme [3, 39, 45] is used to evaluate the inviscid spatial derivatives and first-order Lax-Friedrichs fluxes are used for the building block for higher-order derivative approximations. Time discretization is obtained using a third-order Runge–Kutta scheme.

### 5.1.1 Fifth-Order WENO Scheme—Finite Volume WENO Method

The first WENO scheme was constructed by Liu et al. [46] in the 1994 for a third-order, one-dimensional finite volume. The main idea behind the use of WENO schemes is to combine linearly lower order fluxes or reconstruction to obtain a higher order approximation [46]. WENO uses the idea of adaptive stencils to automatically achieve high-order accuracy and non-oscillatory property near discontinuities. WENO schemes are based on local characteristics decompositions and flux splitting to avoid spurious oscillatory behavior. For multi-dimensional space, WENO schemes were constructed by Jiang and Shu [21] with a general framework for the design of smoothness indicators and nonlinear weights. These schemes are designed based on the successful ENO schemes by Harten et al. in 1987. These schemes are very successful in problems containing both shocks and complicated smooth solution structures, such

as compressible turbulence simulations (similar to the present study), aeroacoustics, convection-dominated problems, Hamilton–Jacobi equations etc.

An important class of homogeneous, hyperbolic equations is known as conservation equations [126]. The general form of such an equation in three-dimensional space is qt + f(q)x + g(q)y + h(q)z = (q) (3.12) where q(x; y; z; t) is a vector of conserved variables.

General non-linear hyperbolic form of conservation equations in three-dimensional space is given by

$$q_t + f(q)_x + g(q)_y + h(q)_z = \psi(q) \tag{5.1}$$

where $q(x,\, y,\, z,\, t)$ is a vector of conserved variables. For one-dimensional scalar conservation laws, Eq. (5.1) simplifies to

$$u_t + f(u)_x = 0 \tag{5.2}$$

Many numerical methods have been developed to solve the above equation. For example, global Lax–Friedrichs (LF) flux splitting [21] discretizes space into uniform intervals of size $\Delta x$. Denoting $x_j = j\Delta x$, the spatial operator of WENO schemes [4], which approximates $-f(u)_x$ at $x_j$, takes the conservative form

$$L = -\frac{1}{\Delta x}(\hat{f}_{j+\frac{1}{2}} - \hat{f}_{j-\frac{1}{2}}), \tag{5.3}$$

where $\hat{f}_{j+\frac{1}{2}}$ is the numerical flux and approximates $h(x_{j+\frac{1}{2}})$ to a high order with $h(x)$ implicitly defined by

$$f(u(x)) = -\frac{1}{\Delta x}\int_{x-\frac{\Delta x}{2}}^{x+\frac{\Delta x}{2}} h(\xi)\, d\xi \tag{5.4}$$

Assume $f(u) \geq 0$ for all $u$ in the range. Therefore, a general flux $f(u)$ can be split into two parts either globally or locally, that is,

$$f(u) = f^{+}(u) + f^{-}(u) \tag{5.5}$$

where $df(u)^{+}/du \geq 0$ and $df(u)^{-}/du \leq 0$. We can just define

$$f^{\pm}(u) = \frac{1}{2}(f(u) \pm \alpha u) \tag{5.6}$$

where $\alpha = \max \mid f'(u) \mid$ and the maximum is taken over the whole relevant range of $u$. All of the above procedure is the global Lax–Friedrichs (LF) flux splitting approach. $\hat{f}^{+}_{j+\frac{1}{2}}$ and $\hat{f}^{-}_{j+\frac{1}{2}}$ are the numerical fluxes obtained from the positive and negative parts of $f(u)$. Thus, we have

$$\hat{f}_{j+\frac{1}{2}} = \hat{f}^{+}_{j+\frac{1}{2}} + \hat{f}^{-}_{j+\frac{1}{2}} \tag{5.7}$$

When $\hat{f}^{+}_{j+\frac{1}{2}}$ and $\hat{f}^{-}_{j+\frac{1}{2}}$ are reconstructed by the WENO method, the Runge–Kutta method can be used to solve the ODE Eq. (5.2).

For discretizing the inviscid terms, two approaches are used. One performs the WENO reconstruction of the flux function using the component-wise approach [3]. Another approach uses characteristics decomposition [41]. Both approaches does dimension-by-dimension reconstruction but for inviscid simulations. Characteristic decomposition takes approximately twice the time as component-wise discretization. Therefore, it is less advantageous for three-dimensional, large-scale simulations.

The dimension-by-dimension reconstruction approach is used to solve the multi-dimensional problem. This reconstruction is carried out mainly by using the WENO fifth-order scheme. WENO methods have been developed to provide robust shock

capturing in compressible turbulence fluid flow and to avoid excessive damping of the fine-scale flow features such as turbulence.

For a multidimensional, chemically reactive algorithm, the right eigenvector matrix $R_m$ is necessary to project flux components onto the characteristic space because of the presence of multiple eigenvalues which is equal to the flow velocity. The following form of the right eigenvector matrix is considered in the present research:

$$R_m = \begin{pmatrix} 1 & 0 & 0 & 0 & 1 & 1 \\ u & 0 & 0 & 0 & u-a & a+u \\ v & 1 & 0 & 0 & v & v \\ w & 0 & 1 & 0 & w & w \\ \frac{1}{2}\left(-2\lambda\tilde{Q}+u^2+v^2+w^2\right) & v & w & -\tilde{Q} & H_0-au & au+H_0 \\ \lambda & 0 & 0 & 1 & \lambda & \lambda \end{pmatrix}, \tag{5.8}$$

where $H_0$ is the total enthalpy. The first four columns correspond to the eigenvalue $u$, while the last two correspond to $u-a$ and $u+a$, respectively.

All the viscous fluxes or terms of the compressible Navier–Stokes equations are discretized using fourth-order central finite differencing schemes [44]. This scheme is designed to be within that of the fifth-order WENO scheme. This central differencing scheme achieves the maximum order of accuracy in the stencil.

For the simulation of shock and homogeneous turbulence interaction, shock-fitting and shock-capturing methods [37, 22, 28] have been used. Shock fitting [40] algorithms treat the shock interface sharply without any dissipation. Hence, they are compatible with low dissipation schemes used for DNS of turbulent flow. At the same time, they have the problem that the shock surface, which is assumed sharp, must be smooth (continuous) and single valued, whereas shock-capturing methods are more

suitable to evaluate problems with large shock front deformations and high preshock $M_t$ values. Nonetheless, shock capturing methods also have some major drawbacks, namely, the reduction of the accuracy of the scheme near the discontinuity, and the presence of spurious oscillations near the shock that pollute the accuracy of evaluated statistical quantities, amongst others.

After careful consideration of all the drawbacks and advantages, the shock capturing (WENO) scheme with the global Lax–Friedrichs flux splitting method was used. This method was validated against the linear theory of the detonation instability growth with particular emphasis on the formation of spurious oscillation at the front. This shock capturing approach is required to be high-order accurate throughout the computational domain to properly simulate the evolution of turbulence.

### 5.1.2 Time Discretization—Third-Order Runge–Kutta Scheme

Time advancement is performed using the compact storage, third-order Runge–Kutta scheme in the present simulation. This semi-discrete time discretization scheme is given by

$$u_t = L(u) \tag{5.9}$$

which is discretized in time by a non-linearly stable, third-order Runge–Kutta time discretization version as follows [47]:

$$u^{(1)} = u^n + \triangle t L(u^n) \tag{5.10a}$$

$$u^{(2)} = \frac{3}{4}u^n + \frac{1}{4}u^{(1)} + \frac{1}{4}\triangle t L(u^{(1)}) \tag{5.10b}$$

$$u^{(n+1)} = \frac{1}{3}u^n + \frac{2}{3}u^{(2)} + \frac{2}{3}\triangle t L(u^{(2)}). \tag{5.10c}$$

/noindent Third-order accuracy in the Runge–Kutta scheme is shown by evaluating $u^{(n+1)}$ Eq. (5.10) above in terms of $u(n)$ where $n$ corresponds to the value of $u$ at the old time, $n+1$ corresponds to the value of $u$ at the new time and $L = \partial u/\partial t$.

# CHAPTER 6

# TEST CASES AND VALIDATIONS

## 6.1 Test Cases for Detonation–Turbulence Interaction

Simulation for detonation–turbulence interaction and shock–turbulence interaction are done to compare them while considering the one-dimensional detonation structure with unit overdrive $f = 1$, specific heat ratio $\gamma = 1.2$, Prandtl number $Pr = 0.72$ and Lewis number $Le = 1$. The heat release parameter (or purely a detonation parameter) $Q$ is independent of the inflow turbulence and is given by

$$\frac{Q_{\rho_\infty}}{p_\infty} = \frac{\gamma(f^2 - 2fM_\infty^2 + M_\infty^4)}{2f(\gamma^2 - 1)M_\infty^2}, \tag{6.1}$$

/noindent A simplification is afforded by letting $f = 1$ (the Chapman–Jouguet condition) and yields the relationship

$$Q \equiv \frac{\tilde{Q}}{p_0/\rho_0} = \frac{\tilde{Q}}{\gamma M_t^2} = \frac{\gamma\,(M^2 - 1)^{\,2}}{2\,(\gamma^2 - 1)\,M^2}, \tag{6.2}$$

where $\tilde{Q}$ is an interaction parameter which depends on the inflow turbulence unlike $Q$ which is independent of the inflow turbulence. The turbulent Mach number $M_t$ is given by

$$M_t \equiv \frac{u_{rms}}{\sqrt{\gamma \frac{p_0}{\rho_0}}} \tag{6.3}$$

Since, all calculations are in the shock reference frame, thus $M > 1$ is the detonation Mach number. For all the cases and calculations, the ratio of the detonation-to-turbulent lengthscale is kept constant and unitary namely:

$$N = \frac{L_{1/2}}{\lambda_0} = 1 \tag{6.4}$$

The Reynolds number based on the acoustic velocity and the reaction half length is given by

$$Re_{L_{1/2}} \equiv \frac{\sqrt{p_0\rho_0}L_{1/2}}{\mu_0} = \frac{Re_\lambda N}{\sqrt{\gamma}M_t} \tag{6.5}$$

For $N = 1$, $M_t \approx 0.2$ and $Re_\lambda$ which is small enough to allow for the numerical simulation of detonation–turbulence interaction problem, $Re_{L_{1/2}} \approx 200$. Equation (6.5) shows that an increase in $N$ leads to a proportional increase in $Re_{L_{1/2}}$, which will require a larger domain size and increased computational requirements as well, see section 6.2.

As shown in Table 6.1 and later discussed in detail, the study consists of a low and a high heat release category. The non-reactive Case IV, that is, the shock–turbulence interaction case, is also classified as a low heat release case for convenience.

/noindent Table 6.1 summarized all the required parameters for the both low and heat release case.

### 6.1.1 High Heat Release Case

In this category, $M = 5.5$ and, correspondingly, the heat release parameter $Q = 38.57$ from equation(6.2). The activation energy $E = 20$ is considered on the basis of a numerical and analytical study [32] done for the detonation structures that are longitudinally stable, that is, stable to one-dimensional perturbations. This

Table 6.1. Description of all the cases considered in the present study

| Case | Low heat release |
|---|---|
| I | Non-forced low heat release |
| II | Entropy-forced low heat release case |
| III | Vorticity-forced low heat release case |
| IV | Non-reactive low heat release |
| | High heat release |
| V | Non-forced high heat release |
| VI | Entropy forced high heat release case |
| VII | Vorticity forced high heat release case |

Table 6.2. Parameters for low and high heat release

| | $M$ | $Q$ | $E$ |
|---|---|---|---|
| High heat release | 5.5 | 38.57 | 20 |
| Low heat release | 4 | 19.18 | 12 |

is because longitudinal instability gives rise to axial motion of the mean shock front and galloping waves [48], which complicate the evaluation of the ensemble average as a space–time mean at fixed axial distances from the shock. The longitudinal instability boundary divides the $E$–$Q$ quarter plane into two regions as shown in the figure 6.1 [33] for $\gamma = 1.2$ and $f = 1$. The activation energy is responsible for the changes observed in the induction time with the post shock temperature in von Neumann conditions $(\partial \ln \tau_i / \ln T_{ps})_{f=1}$ where $\tau_i$ is the induction time and $T_{ps}$ is the postshock temperature [35]

For the high heat release category, three cases were considered, namely, non-forced, entropy forced and vorticity forced. For vortical forcing, three-dimensional isotropic velocity perturbations evaluated at constant pressure, density and $\lambda$ are obtained from the decay of the homogeneous turbulence. For entropy forcing, the

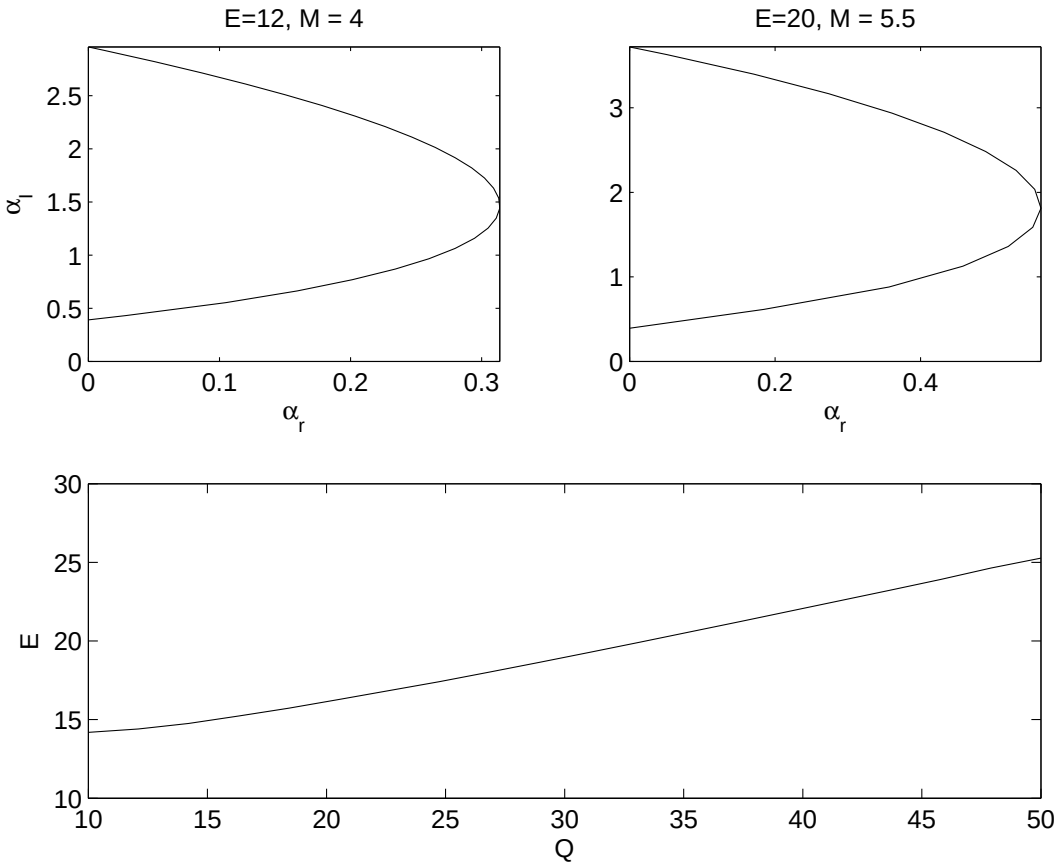


Figure 6.1. Longitudinal instability boundary for the detonation structures for both the high and low heat release case ($\gamma = 1.2$ and unit overdrive $f = 1$).

vortical waves are nullified in favor of entropy waves which are obtained by using the Morkovin scaling [29]. Entropy forcing features density perturbations evaluated at constant pressure, velocity and $\lambda$. Density perturbations in the constant pressure inflow are related to the isotropic turbulence velocity perturbations by

$$\frac{\rho'}{\bar{\rho}} = (\gamma - 1)M^2 \frac{u'}{\bar{u}}. \tag{6.6}$$

Also, temperature fluctuations in the constant pressure inflow are given by

$$\frac{\rho'}{\bar{\rho}} = -\frac{u'}{\bar{u}} \tag{6.7}$$

/noindent Thus, density perturbations are opposite to those of temperature perturbations in a constant pressure field. Finally, the non-forced simulation corresponds to conditions obtained by removing incoming turbulence so that only natural instability fluctuations are present in the postshock field.

### 6.1.2 Low Heat Release Case

The second category considered is the low heat release where the inflow Mach number $M = 4$ and, correspondingly, the heat release parameter $Q = 19.18$. The activation energy $E = 12$ was chosen on the same basis as that above for the high heat release case. For low heat release, four simulations were performed: reactive with vortical forcing, reactive with entropic forcing, non-reactive and non-forced. Here, the non-reactive case corresponds to shock–turbulence interaction and is added unlike for the high heat release case. The same conditions and methods are applied for the reactive (vorticity and entropy forced) and non-forced case as for the high heat release cases.

## 6.2 Verification/Validation

All the above test cases for the high and low heat release are validated against linear and inviscid growth rate results while considering all the numerical methods, approaches and conditions for the problem. The following parameters are kept constant $\gamma = 1.2$, $f = 1$, $E = 12$, $Q = 19.18$ and $kL_{1/2} = 1$, where $k$ is the spatial frequency constant for all the cases. The verification and validation are as follows:

**Case I:** LF component-wise approach is used to solve the Euler equations on a stretched grid of dimensions $500 \times 101$.

**Case II:** Same LF component-wise approach as for Case I to solve the Euler equations on a stretched grid but of different dimensions $1000 \times 201$.

**Case III:** WENO-LF component-wise is used to solve the Navier–Stokes equations on a stretched grid of dimensions $500 \times 101$ with Reynolds number $Re_{L_{1/2}} = 150$.

**Case IV:** WENO-LF characteristic-wise approach is used to solve the Navier–Stokes equations on a stretched grid of dimensions $500 \times 101$ with Reynolds number $Re_{L_{1/2}} = 150$.

**Case V:** Same approach is implemented as for Case IV (WENO-LF characteristic wise), but for solving the Euler equations instead of the Navier–Stokes equations on the same stretched grid size.

The results of the verification and validation [33] for the first four cases are shown in Fig. 6.2. In the figure, the solid line represents the maximum value of the $v$ velocity component perturbation for the linear, inviscid analysis and the broken lines represent the nonlinear analysis. Thin broken lines represent the maximum value of the cross-wise sine transform of the computed solution while the thick ones represent the spatial maximum of the "$u$" velocity perturbation.

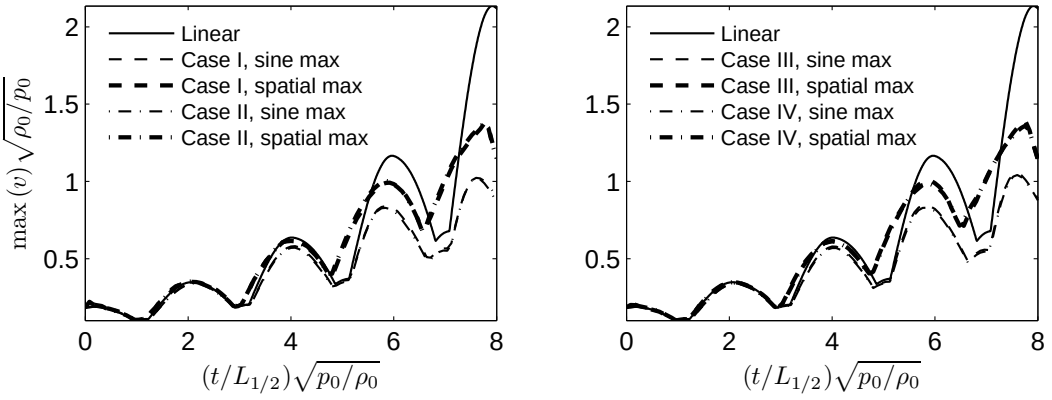


Figure 6.2. Linear and non-linear instability growth from a normal mode solution for the all four different cases I, II, III and IV.

From the analysis of the first four cases, it is concluded that for three-dimensional viscous simulations, the discretization error is small compared to the linearization error for the grid and the stretching conditions. Also, viscosity has a marginal effect on the instability as well as on the nonlinear evolution.

Case I and case V involve two different types of reconstruction strategies, namely, one for component-wise and other for characteristic-wise. Inviscid solutions [33] obtained from both cases are shown in the figure 6.3. A large difference between the maximum of the $y$ sine transform and spatial maximum is noticed in the Fig. 6.3. It is concluded that there are more severe spurious oscillations in the characteristic reconstruction strategy which lead to significant loss of the accuracy in the simulation. But this conclusion is antithetical to one-dimensional detonation simulations showing accuracy improvements as a result of characteristic reconstruction.

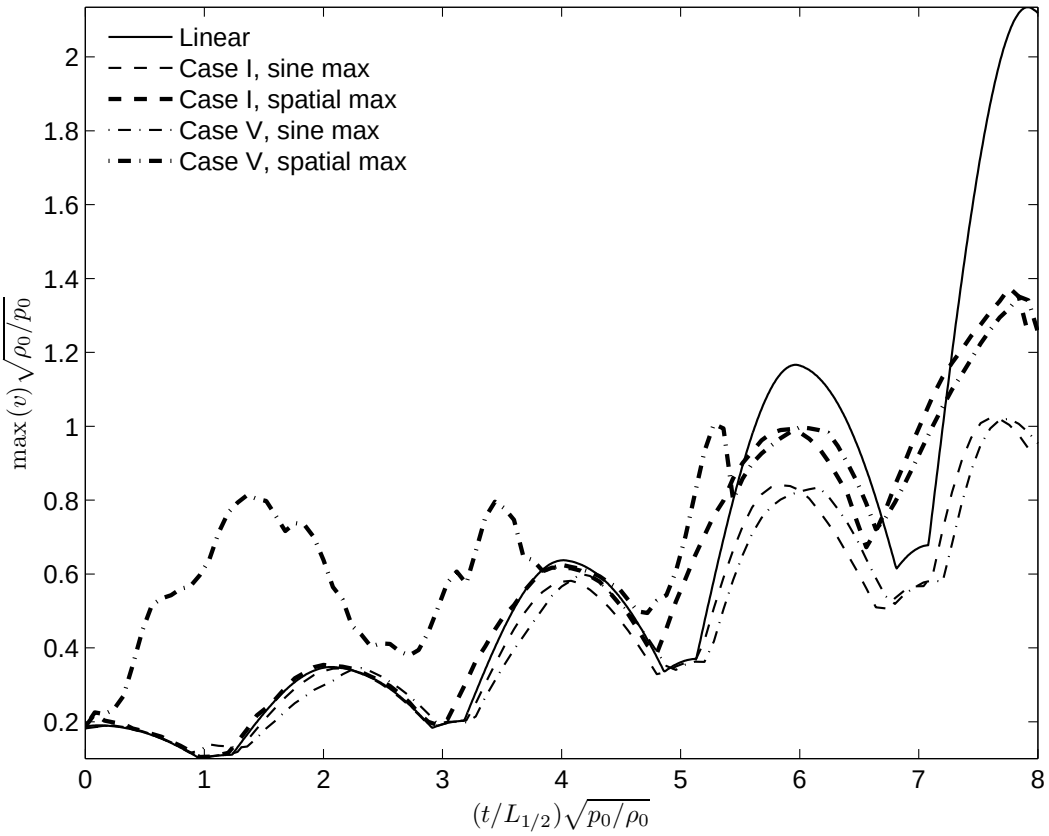


Figure 6.3. WENO reconstruction strategies effect on the growth of normal mode disturbances for Cases I and V.

# CHAPTER 7

# RESULTS AND ANALYSIS

This chapter examines the evolution of the rms of the velocity (the square of which is called the variance) and the spatial auto-correlation of the longitudinal velocity fluctuations for the detonation–turbulence interaction.

## 7.1 Space–Time Ensemble Averaging

In general, space–time ensemble averaging can be used to provide statistical descriptions of random data. The velocity fluctuations at a given point in space $\vec{x}$ and time $t$ in a turbulent flow is given by $u_i(\vec{x},\, t)$, where $u$ is a random variable. Given a large number of identical conditions so that $u_i^{(n)}(\vec{x},\, t)$ in each of them is identically distributed, then the ensemble averaging of $u_i^{(n)}(\vec{x},\, t)$ is given by

$$\langle u_i(\vec{x},\, t)\rangle = U_i(\vec{x},\, t) \equiv \lim_{N\to\infty} \frac{1}{N} \sum_{n=1}^{N} u_i^{(n)}(\vec{x},\, t) \tag{7.1}$$

where $U_i(\vec{x},\, t)$ is the ensemble averaged value of $u_i(\vec{x},\, t)$ with the independent variables $\vec{x}$ and $t$.

Velocity fluctuations $u_i'(\vec{x},\, t)$ are considered as a random variable. They are given by

$$u'(\vec{x},\, t) = u(\vec{x},\, t) - U(\vec{x}) \tag{7.2}$$

From above relationship, the average of the velocity fluctuation for a stationary field is zero, that is,

$$\langle u' \rangle = 0 \tag{7.3}$$

However, the ensemble average of the square of the velocity fluctuations called the velocity variance and denoted by var$[u]$ or $\langle u'^2 \rangle$ is not zero, where

$$\text{var}[u(\vec{x})] \equiv \langle (u'(\vec{x},\, t)^2 \rangle = \langle [u(\vec{x},\, t) - U(\vec{x})]^2 \rangle = \lim_{N \to \infty} \frac{1}{N} \sum_{n=1}^{N} u_n^2 - U^2 \tag{7.4}$$

A proper estimate of averages requires a large ensemble. In practice, one strives to obtain large datasets and Eq. (7.4) is now rewritten as

$$\text{var}[u(\vec{x})] = \langle u^2(\vec{x}) \rangle - U^2 \tag{7.5}$$

The standard deviation of $u(\vec{x},\, t)$ is the square root of the variance, namely,

$$\sigma_u(\vec{x}) = +\sqrt{\text{var}[u(\vec{x})]} \tag{7.6}$$

The standard deviation is also known as the rms value. For a weakly stationary distribution, the mean and the standard deviation (or variance) are constant. Second order moment minus the square of the first order moment (mean) gives the ensemble mean which is called as first moment and also, called as the second central moment of $u$ due to the implication that the mean has been subtracted off before squaring and averaging. Variance is also called as the standard deviation of the random variable $u$. Further, of interest in statistical studies of turbulence are the the third and fourth standardized central moments of the velocity derivatives (skewness and kurtosis respectively), given by

$$S_u = \langle (\partial u/\partial x)^3 / [\overline{(\partial u/\partial x)^2}]^{3/2} \rangle \tag{7.7}$$

$$K = \langle (\partial u/\partial x)^4 / [\overline{(\partial u/\partial x)^2}]^2 \rangle \tag{7.8}$$

Temporal decay simulation is started with a solenoidal velocity field $\nabla \cdot \vec{u} = 0$, zero pressure and density fluctuations, a turbulent Mach number $M_t = 0.235$, and a fluctuation Reynolds number

$$Re_\lambda \equiv \frac{\rho_0 u_{rms} \lambda}{\mu_0} = 100 \tag{7.9}$$

The fluctuation Reynolds number is plotted in the upper left panel of Fig. 7.1 against the nondimensional time $t$.

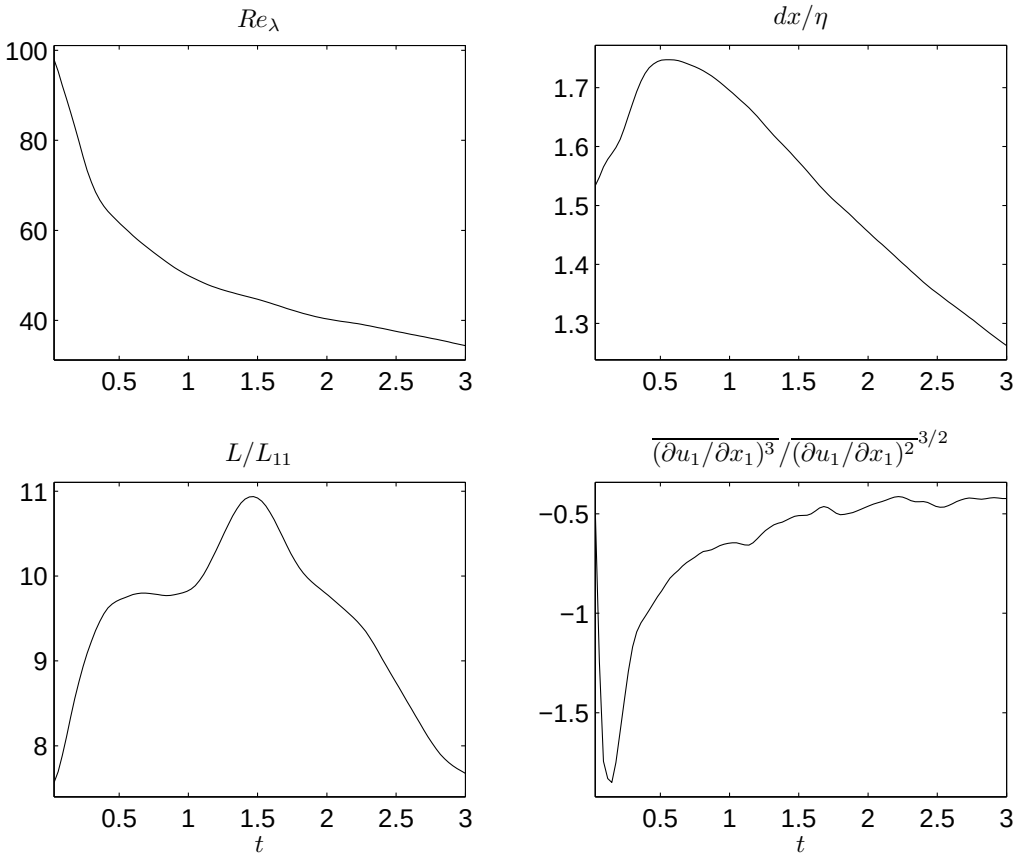


Figure 7.1. Fluctuation Reynolds number, evolution of $S_u$, and the ratio of length scales $\triangle x/\eta$ and $L/L_{11}$ are plotted against the non-dimensional time $u_{rms}/\lambda_{t=0}$.

The temporal decay of the isotropic turbulent field is stopped when the velocity derivative skewness $S_u$ stabilizes close to the value of $-0.5$ [31]. The evolution of $S_u$ is plotted against non-dimensional time $t = u_{rms}/\lambda_{t=0}$ in the bottom-right panel of Fig. 7.1. The ratio between the uniform grid spacing $\triangle x$ and the Kolmogorov length scale $\eta$ and the ratio between the computational box size $L$ and the integral length scale $L_{11}$ are also shown against the non-dimensional time in the right top plot and bottom left respectively to validate our assumptions. The above considerations satisfy all the typical requirements for the resolution of the small scales and the spatial correlations, that is, $\triangle x/\eta < \pi/1.5 \approx 2.1$ and $L/L_{11} > 2\pi/0.8 \approx 7.85$.

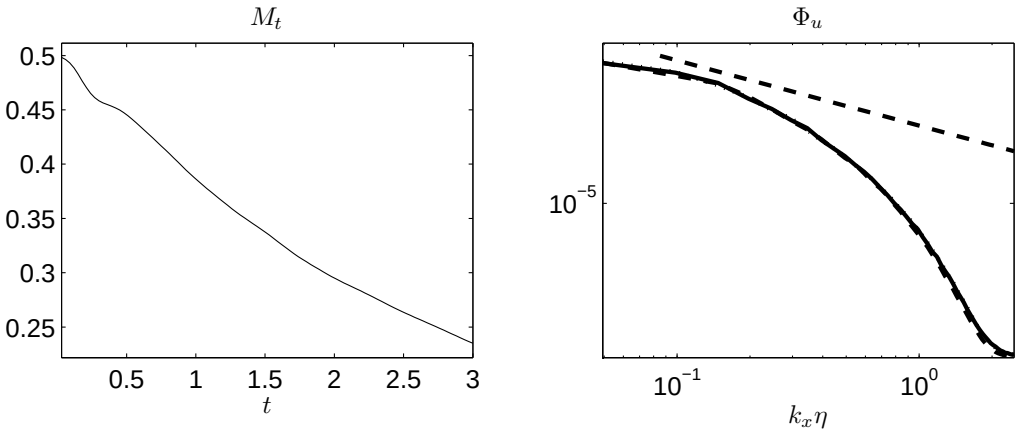


Figure 7.2. Time decay of homogeneous, isotropic turbulence starting from a solenoidal field (Mach number and one-dimensional energy spectrum).

As can be seen in Fig. 7.2, when $t = 3$, $M_t = 0.235$. Spatial realization [33] is used to model the inflow boundary conditions using data from this instant. Accordingly, the decayed turbulence is rescaled; length and velocity are rescaled to the Taylor microscale $\lambda$ and the velocity rms respectively. This process is carried out by advecting the random spatial realization by assuming frozen dynamics.

The longitudinal energy spectrum is given by

$$\Phi_u(k_x) = \sum_{k_y,k_z} \mathcal{F}_{k_x,k_y,k_z}(u')\mathcal{F}_{k_x,k_y,k_z}(u')^* \tag{7.10}$$

where $\mathcal{F}_{\vec{k}}$ is the three-dimensional Fourier transform.

The right side of Fig. 7.2 shows the longitudinal energy spectrum. The thick line in the right indicates the Kolmogorov $k^{(-5/3)}$ law.

## 7.2 Analysis of Velocity Variances/Root Mean Square Velocity

The velocity variance $\overline{u'^2}$ is an important parameter of the statistical measure for the turbulent flow. The preshock turbulent field is homogeneous and isotropic which can be characterized by the velocity variances or the rms value, such as $u_{rms} = \sqrt{\overline{u'^2}}$ , the Taylor microscale based on the dissipative function $\lambda_0$, the preshock turbulence unperturbed density $\rho_0$ and the gas constant $R$. The flow Reynolds number is based on the acoustic velocity and the reaction half length $L_{1/2}$ and given by

$$Re_{L_{1/2}} \equiv \frac{\sqrt{p_0\rho_0}L_{1/2}}{\mu_0} = \frac{Re_\lambda N}{\sqrt{\gamma}M_t} \tag{7.11}$$

where $N = 1$ is the ratio of the reaction half length and the Taylor microscale. Flow Reynolds number is set to $Re_{L_{1/2}} = 200$.

$$M_t \equiv u_{rms}/\sqrt{\gamma p_0/\rho_0} \tag{7.12}$$

$M_t$ is the turbulent Mach number which is set to 0.235 and

$$Re_\lambda \equiv \rho_0 u_{rms}\lambda/\mu_0 \tag{7.13}$$

Table 7.1. Half-length $\overline{L}_{1/2}$ for different simulations.

| Case | | $\overline{L_{1/2}}$ |
|---|---|---|
| I | Non-forced low heat release | 1.840 |
| III | Vorticity-forced low heat release | 1.542 |
| V | Non-forced high heat release | 1.963 |
| VI | Entropy-forced high heat release | 1.889 |
| VII | Vorticity-forced high heat release | 2.312 |

is the Reynolds number based on the Taylor microscale which is equal to 100. The reaction half-length supported by turbulent inflow $\overline{L}_{1/2}$ is estimated and evaluated using the mean profile distance between $\overline{\lambda} = 10^{-3}$ and $\overline{\lambda} = 0.5$. The reaction half-length for the different cases are listed in Table 7.1.

Intrinsic and forced fluctuations significantly affect the mean flow structure. The ratio of the intrinsic-to-forced length scales mainly depends on the nondimensional parameter $N$ as defined earlier. If $N$ varies from unity then it will have a strong effect on the scales behind the detonation structures [33]. Using the Rankine–Hugoniot theory and conditions, the jump across the shock is lower than that predicted for all the above reactive and non-reactive cases as shown in the figures below of velocity variances. This phenomenon is the due to the consequence of both shock front motion and the corrugation which are consistent with the mean shock profiles in all the cases. Forced and non-forced spectra show marked differences in the responses of reactive and nonreactive configurations to the inflow turbulence. These differences are investigated in detail by analyzing the variances of the fluctuation using space–time ensemble averaging as discussed above in section 7.1 at fixed distances from the shock. The rms velocity fluctuations downstream of the detonation wave ($u_{rms},\ v_{rms},\ w_{rms}$) are considered for the seven different cases. The velocity fluctuations are ensembled averaged for $\{n = 100,\ 200,\ 1\}$ .

### 7.2.1 Low Heat Release Cases

In these cases, the interaction is analyzed where the inflow turbulence Mach number equals to $M = 4$ with the heat release parameter $Q = 19.18$ and activation energy $E = 12$. Four different simulations are analyzed for the low heat release case: non-forced, vorticity-forced, entropy-forced and non-reactive.

#### 7.2.1.1 CASE I: Non-Forced Low Heat Release Case

This case is for the non-forced interaction where there is no initial turbulence. Thus, only natural instability fluctuations are present in the postshock field. The shock location is approximately at $X = 0$ where $X$ is the streamwise distance normalized by the reaction half-length because there is no incoming turbulence. Since the flowfield is globally nonstationary, ensemble averaging of ($u'$, $v'$, $w'$) is done at each $X$ location for $\{n = 100, 200, 1\}$ datasets to yield ($u_{rms}$, $v_{rms}$, $w_{rms}$). In other words, the computations generated an ensemble of 100 datasets. At each $X$ location, 100 datasets, starting from the 100th one, is averaged to obtain $\vec{u}_{rms}$. Figure 7.3 shows the spanwise rms velocity distributions.

The figure shows a rapid increase in $u_{rms}$ just ahead of the mean shock location, resulting in a departure from isotropy. This increase is more rapid in the streamwise direction than the spanwise directions due primarily to the longitudinal instability of the shock front. It can be seen that isotropy is maintained in the spanwise plane. The streamwise fluctuations decay rapidly after the shock and a return to isotropy occurs around $X = 1.5$. Despite the return to isotropy, significant velocity fluctuations remain even to the exit of the computational domain.

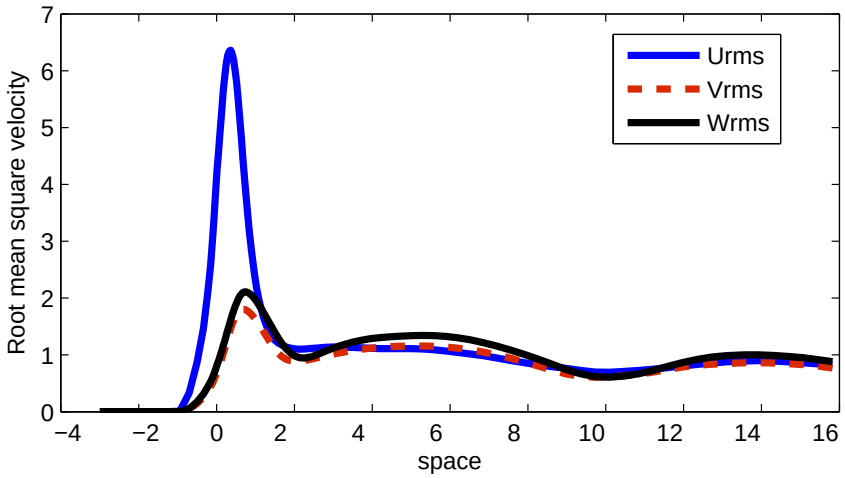


Figure 7.3. RMS of velocity perturbations ($u'$, $v'$, $w'$) along the $X$ direction for the non-forced, heat release case ($M = 4$).

#### 7.2.1.2 CASE II: Entropy-Forced Low Heat Release Case

In this case, vortical waves are nullified in the favor of entropy waves which are obtained by using Morkovin scaling Eq.(6.1). This case features a density perturbation evaluated at constant pressure, constant velocity and a constant $\lambda$. Entropy forcing leads to the increase in the reaction half-length $\overline{L_{1/2}}$. The rms velocity distribution for this case is shown in Fig. 7.4. The longitudinal distance is normalized by the Taylor microscale of the incoming turbulent field.

Similar observations as for the nonreactive Case I can be made of the rms velocity distributions. There is a statistically insignificantly higher value of $v_{rms}$ after the shock. The rms distribution shows a rapid return to isotropy and a residual level of disturbances remain at the exit of the computational domain.

#### 7.2.1.3 CASE III: Vorticity-Forced Low Heat Release Case

In this case, vortical waves are propagated by the decay of the initial, homogeneous, isotropic turbulence at $M = 4$. This vortical forcing consists of the three-

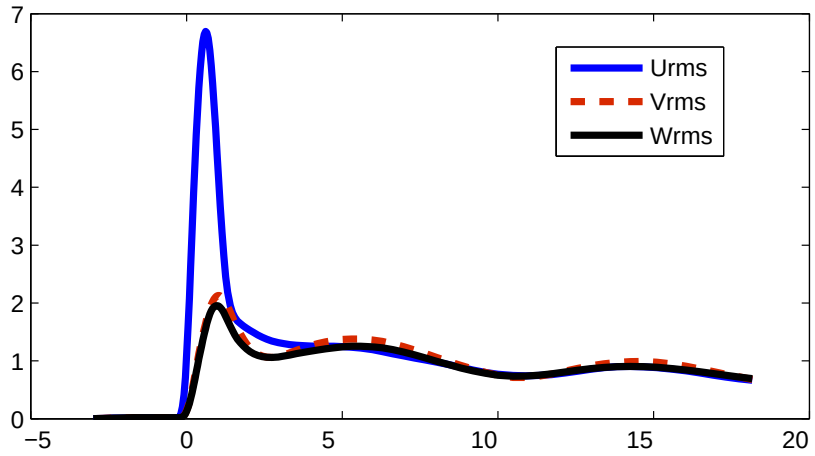


Figure 7.4. RMS of velocity perturbations ($u'$, $v'$, $w'$) along the $X$ direction for the entropy-forced, low heat release case ($M = 4$).

dimensional isotropic velocity perturbations at constant pressure, constant density, and constant $\lambda$. For this case, $\overline{L_{1/2}} = 1.542$. The rms velocity components are plotted in Fig. 7.5.

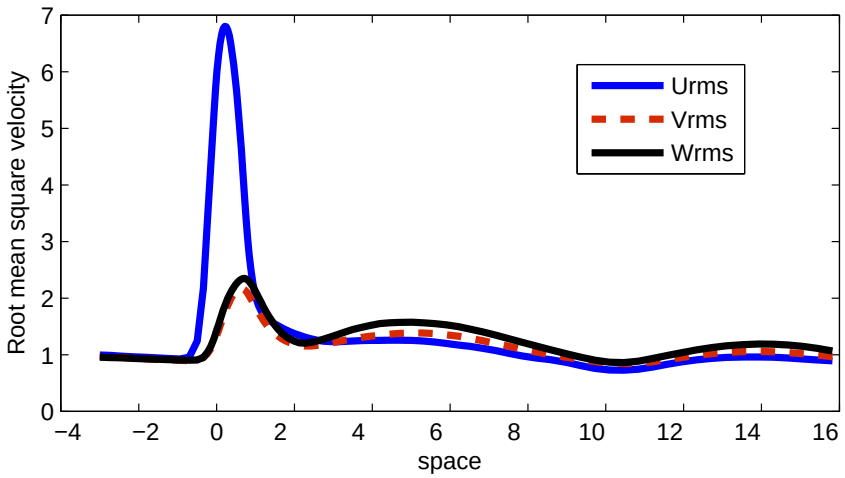


Figure 7.5. RMS of velocity perturbations ($u'$, $v'$, $w'$) along the $X$ direction for the vorticity-forced, low heat release case ($M = 4$).

Similar trends as for Cases I and II are observed in this figure. However, due to the presence of an initial fluctuating vorticity field, the incoming rms velocity distribution is not negligible but has a value just under unity. The postshock rms velocity distribution returns to the initial, quiescent level of around unity at $X \approx 2$. This rapid decay is attributed to the fact that vorticity forcing is weaker than entropy forcing and thus does not affect the postshock perturbation dynamics as much.

#### 7.2.1.4 CASE IV: Non-Reactive Case

This case is simply the more widely studied shock–turbulence interaction. Significant differences are observed between this case and Cases I–III that involve heat release. The rms velocity distribution is shown in Fig. 7.6. The transverse rms behavior in either the $y$ or $z$ direction is exactly the same. The longitudinal rms velocity peak is less than the reactive cases discussed previously. Moreover, the peak appears ahead of the mean shock location. This has been observed because there is no chemical activity involved in the simulation and also due to the decay of the sub-critical acoustic wave (Sub-critical acoustic waves are the waves which are damped in the postshock far-field region) which is followed by the viscous dissipation. Local maxima in the figure (7.6)is also observed due to the above mentioned effects.

### 7.2.2 High Heat Release Cases

#### 7.2.2.1 CASE V: Non-Forced High Heat Release Case

The rms velocity distributions are shown in Fig. 7.7. Compared to the low heat release cases, the peak value of $u_{rms}$ is now about 8.5 compared to under 7. The rms values drop from the peak very rapidly, leveling off at about $X = 3$. The downstream

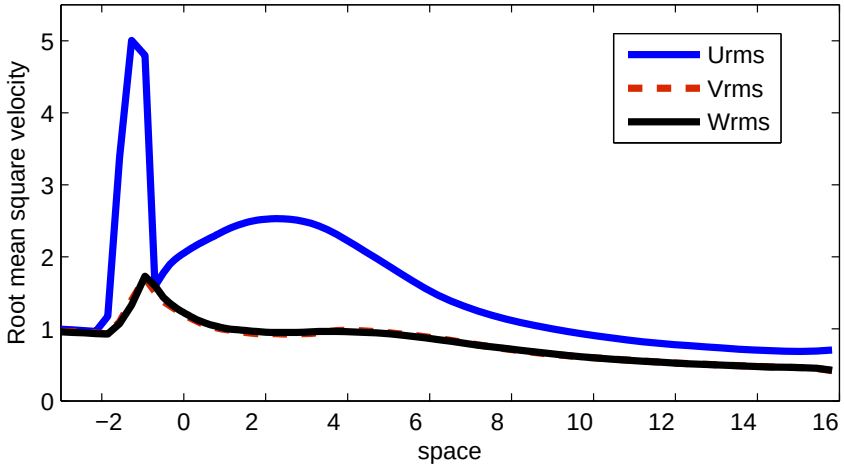


Figure 7.6. RMS of velocity perturbations ($u'$, $v'$, $w'$) along the $X$ direction for the non-reactive case ($M = 4$).

rms values are higher than the low heat release case and remain till the exit of the computational domain. The return to isotropy happens later at about $X = 10$.

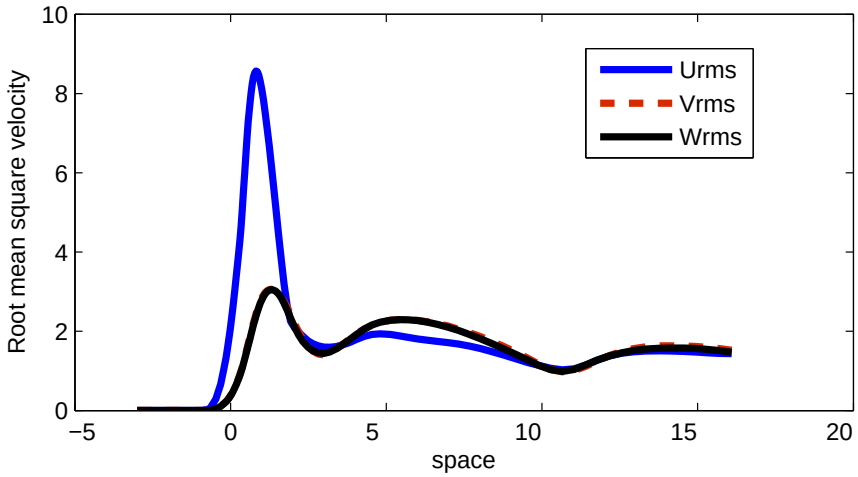


Figure 7.7. RMS of velocity perturbations ($u'$, $v'$, $w'$) along the $X$ direction for the non-forced high heat release case ($M = 5.5$).

#### 7.2.2.2 CASE VI: Entropy-Forced High Heat Release Case

The rms velocity distributions are shown in Fig. 7.8. Unlike the unforced case, the peaks decay more slowly. The transverse rms velocity fluctuations are isotropic but the entire rms distribution does not attain isotropy until $X \approx 5$. This is later than the unforced case. For the high heat release case at $M = 5.5$, entropic perturbations are more effective in reducing the peak intensities compared to the vortical perturbations as observed in the later case. It is also more effective in reducing the integral scales and the longitudinal velocity fluctuations associated with the detonation instability and the postshock transverse fluctuations.

Entropic forcing leads to an increased probability of high temperature fluid in the reaction zone; therefore, possibility of formation of hot spots at higher activation energy is higher than the low heat release case.

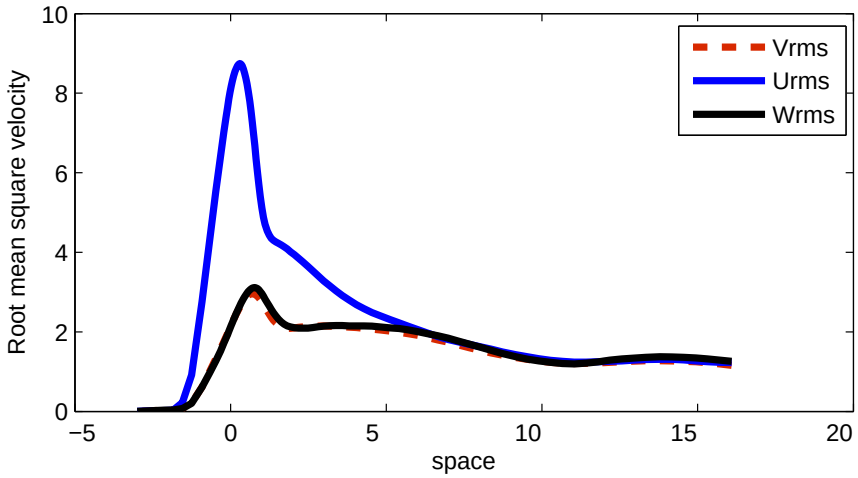


Figure 7.8. RMS of velocity perturbations ($u'$, $v'$, $w'$) along the $X$ direction for the entropy-forced, high heat release case ($M = 5.5$).

#### 7.2.2.3 CASE VII: Vorticity-Forced High Heat Release Case

The rms velocity distributions are shown in Fig. 7.9. Vorticity forcing ahead of the wave tends to reduce the region of heat release with more significant effect especially for the low heat release case while comparing with the high heat release case.

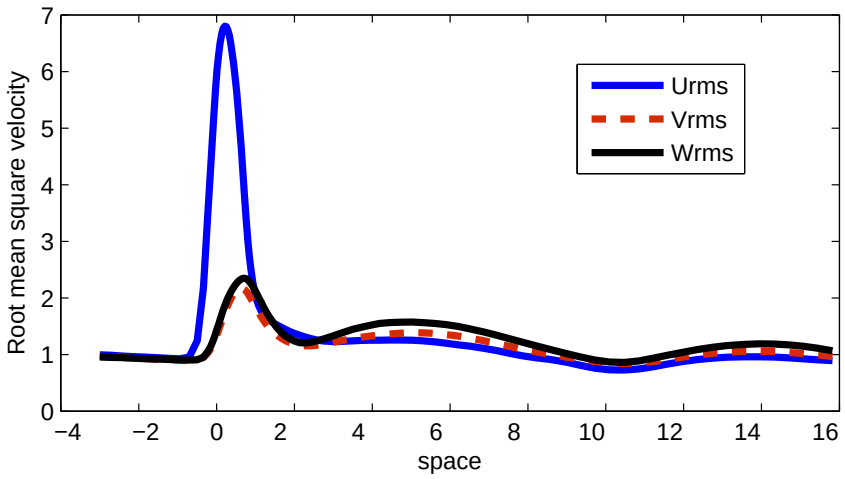


Figure 7.9. RMS of velocity perturbations ($u'$, $v'$, $w'$) along the $X$ direction for the vorticity-forced, high heat release case ($M = 5.5$).

Jamme et al. [20] investigated turbulence behavior across a shock and the influence of the incoming turbulence on the interaction. They computed fluctuating vorticity variances and showed that the baroclinic torque is responsible for the production of transverse vorticity. More reduction in the transverse Taylor microscale and the integral scale is observed compared to the longitudinal Taylor microscale where there is no significant changes occur in the Fig. 7.10. Strong influence of preshock density fluctuations are observed on the postshock perturbation dynamics [31]. In Figure 7.10, longitudinal and transverse velocity fluctuations for different inflow Mach number and parameters are shown (all the simulation cases).

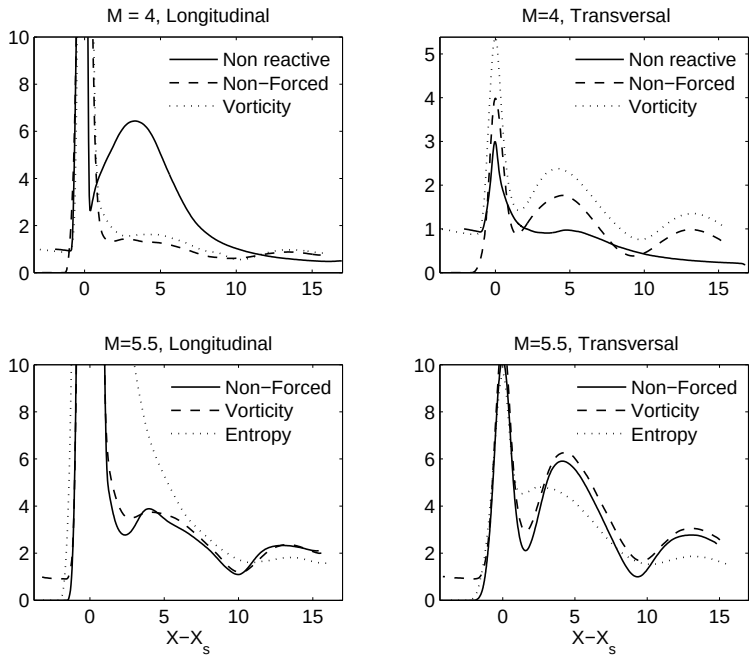


Figure 7.10. Transverse and longitudinal velocity perturbations for different inflow the ($x$, $y$, $z$) directions for each simulation.

In Fig. 7.10, both the low and high heat release cases are shown along with the different inflow perturbations. The dotted line represents vortical and entropy forcing, solid line represents the non-reactive case and dashed lines represents the non-forced case for two different in flow mach number.

The longitudinal and transverse velocity Taylor microscales $\lambda_1$ and $\lambda_2$ are also examined both for the high and low heat release cases to help in the understanding of the velocity perturbations presented in Fig. 7.10. The Taylor microscales $\lambda_1$ and $\lambda_2$ are defined by

$$\lambda_1 = \sqrt{\frac{\overline{u'^2}}{\overline{(\partial u'/\partial x)^2}}}, \quad \lambda_2 = \sqrt{\frac{\overline{v'^2}}{\overline{(\partial v'/\partial y)^2}}} \tag{7.14}$$

while the local turbulent Mach number is given by

$$M_t = \frac{\sqrt{\overline{|\vec{u}| - \overline{|\vec{u}|}^2}}}{\overline{\sqrt{\gamma p/\rho}}}, \tag{7.15}$$

In the analysis, we also compared and analyzed the effect of low and high turbulent Mach number at $M = 0.1$ and $M = 0.235$ respectively on the velocity fluctuations as shown in the figure 7.11.

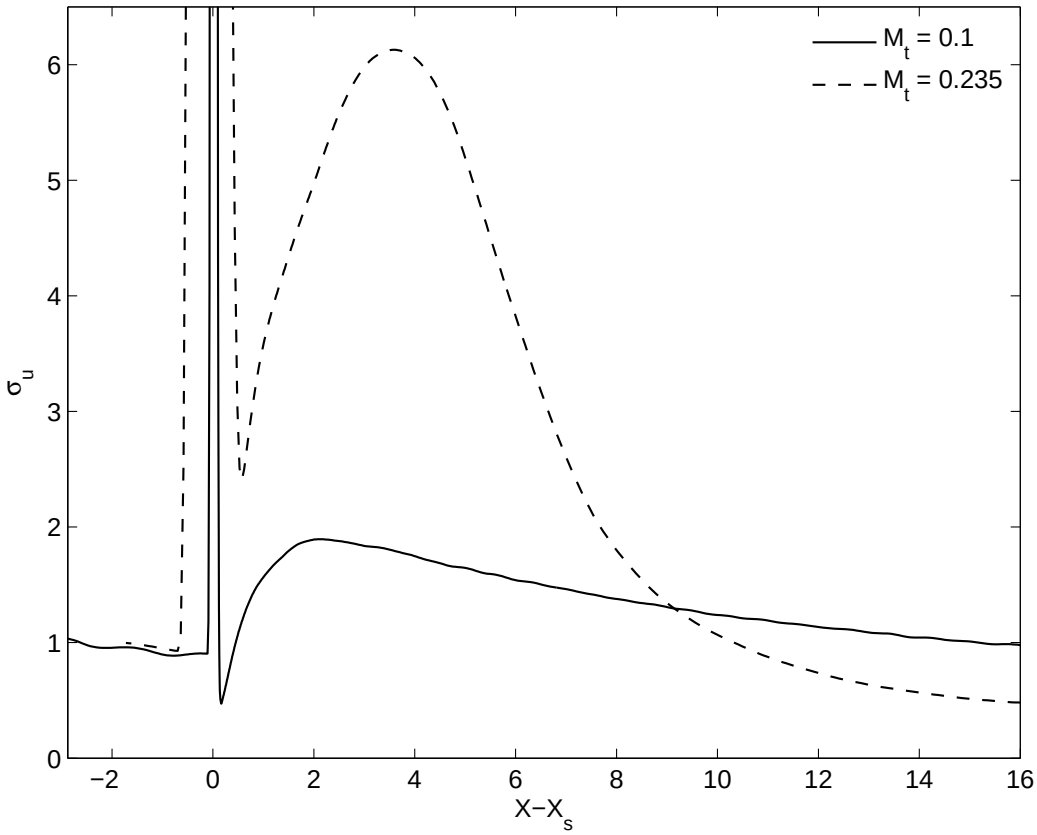


Figure 7.11. Comparison of effects of the low and high turbulent Mach number on the velocity perturbations at Mach number $M = 4$.

From the discussion above, it can be concluded that the non-reactive case exhibits a drop in the rms velocity immediately after the shock followed by recovery due to the pressure work. Entropic fluctuations also lead to a larger $M_t$ immediately after the shock compared to the vortical fluctuations [33] . Reactivity strongly reduces the turbulent Mach number immediately after the shock while the addition of inflow fluctuations weakly affects the $M_t$ in the reactive case as shown in Fig. 7.11.

## 7.3 Averaged Space-Time Auto-Correlation

The preshock turbulent field is homogeneous and characterized by velocity fluctuations. In the DNS [7] of the interaction of Mach 1.5 shock wave with turbulent shear flow, where it was concluded that the sign and magnitude of the correlation between the velocity and the temperature fluctuations have a crucial influence on the kinetic energy amplifications across the shock. Massa et.al. [35] applied linear analysis to detonation–turbulence interaction, as a natural extension of previous shock–turbulence interaction analysis. A selective wave amplification was found which is based on the ratio of the turbulence lengthscale and the reaction half length. The decay of freely evolving two-dimensional isotropic turbulence was studied by Lowe and Davidson [30] where they showed that periodic boundary conditions impose mirror image, long range correlations of velocity and the vorticity. Also they concluded that these correlations have the potential to influence the dynamical behavior of the turbulence. The autocorrelation function of stationary random data describes the general dependence of the values of a parameter of the dataset at one time on the values of the same parameter at another time. The discrete version of the autocorrelation coefficient which is the autocorrelation function normalized by the variance for the random variable $u_i'$ can be written as

$$r_{u'u'}(x) \triangleq \frac{\sum_i u_i'^2}{\overline{u'^2}} \in \{-1,\, 1\} \tag{7.16}$$

The auto-correlation function is simply a two-point correlation function, $r_{u'u'}(x) = \langle u_x(x) u_x(x+r) \rangle$. Autocorrelation [8] helps in differentiating between the small and large scale eddies in turbulence, and is preferable to one-dimensional, scalar functions, such as $u_x$.

Table 7.2. Nine different locations in the streamwise direction for the autocorrelation for all the seven simulations

| Location ID | Grid Location | Distance from the shock normalized by $\lambda$ |
|---|---|---|
| 1 | 2 | 16.0927 |
| 2 | 64 | 11.3377 |
| 3 | 127 | 6.7859 |
| 4 | 189 | 3.4199 |
| 5 | 251 | 1.6249 |
| 6 | 313 | 0.8538 |
| 7 | 376 | 0.3526 |
| 8 | 438 | $-0.1330$ |
| 9 | 500 | $-3$ |

The correlation coefficients at selected streamwise locations are ensemble averaged. One hundred correlation coefficients at nine selected streamwise locations are ensemble average, in a similar manner as that used for obtaining the averaged rms velocities discussed previously in sections 7.2.1 and 7.2.2. The nine locations are shown in Table 7.2. There is clustering near the shock location due to the steeper gradients that were see in the rms velocity distribution. One point is chosen ahead of the shock for reference. In Table 7.2, the grid location refers to the streamwise grid points of which there are 500. These grid point locations are referenced to a distance from the shock, normalized by the Taylor microscale $\lambda$ ahead of the interaction, except for the nonforced cases where normalization is by the reaction half-length.

### 7.3.1 Low Heat Release Case

#### 7.3.1.1 CASE I: Non-Forced Low Heat Release Case

Figure 7.12 shows the autocorrelation coefficients for the nine locations starting from the top left and ending at the bottom right. The autocorrelation ahead of the interaction shows a circular shape but evolves into a diamond shape downstream of

the interaction. It is thought that the diamond shape arises from the imposition of periodic and reflecting boundary conditions on the lateral boundaries [9]. The boundaries create transverse waves that are present due to the square or rectangular boundaries and that are usually visualized as cellular structures. Thus, one expects a correlation arising from these structures. As to be expected, slightly negative regions occur further from the peak but the autocorrelations decay to zero further away may be!

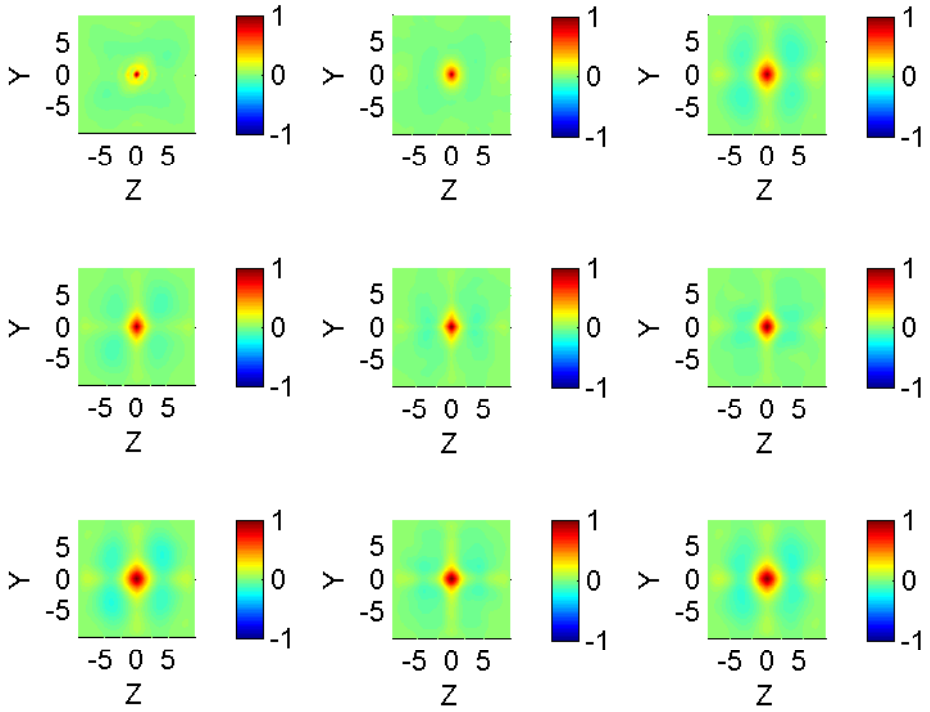


Figure 7.12. Autocorrelation coefficients of $u'$ for the non-forced low heat release case ($M = 4$).

#### 7.3.1.2 CASE II: Entropy-Forced Low Heat Release Case

Figure 7.13 shows an extremely small correlation peak upstream of the interaction that grows due to shock interaction. As in Case I, the autocorrelation takes on a diamond shape but in this case the major axis is horizontal. No reasons can be offered at the moment as to why the orientation is different between Cases I and II.

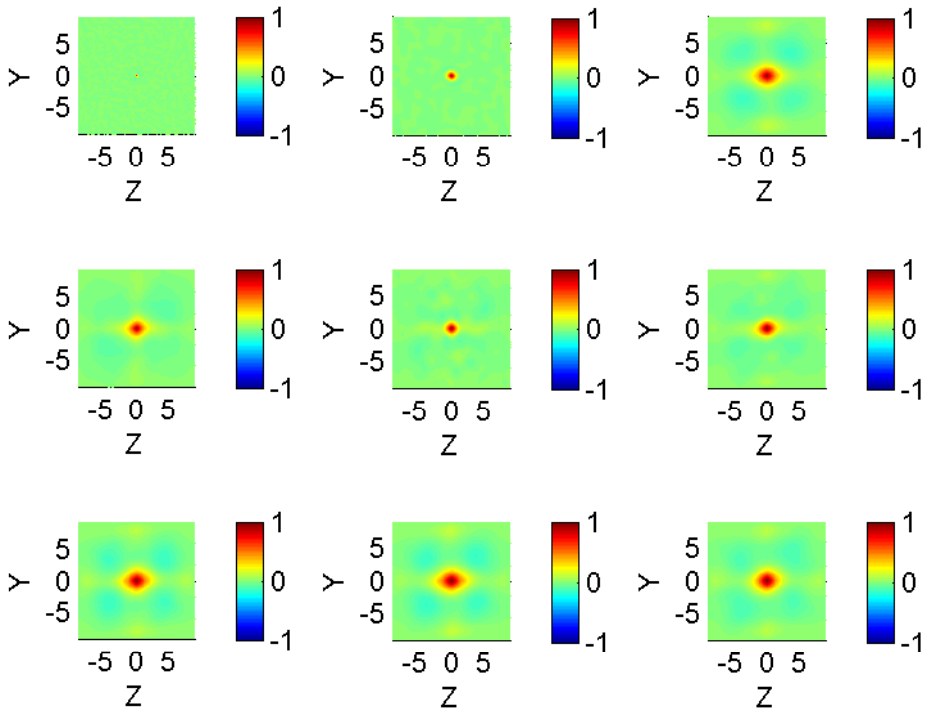


Figure 7.13. Autocorrelation coefficients of $u'$ for the entropy-forced low heat release case ($M = 4$).

#### 7.3.1.3 CASE III: Vorticity-Forced Low Heat Release Case

The autocorrelation coefficients for this case are shown in Fig. 7.14. Due to the presence of initial fluctuations ahead of the shock, the autocorrelation shows a larger circular shape than in Case II. Downstream of the shock, the autocorrelation appears squarish at $X = 0.3526$ but becomes smeared and slightly irregular further downstream. However, further downstream, the autocorrelation takes on a vertical diamond shape.

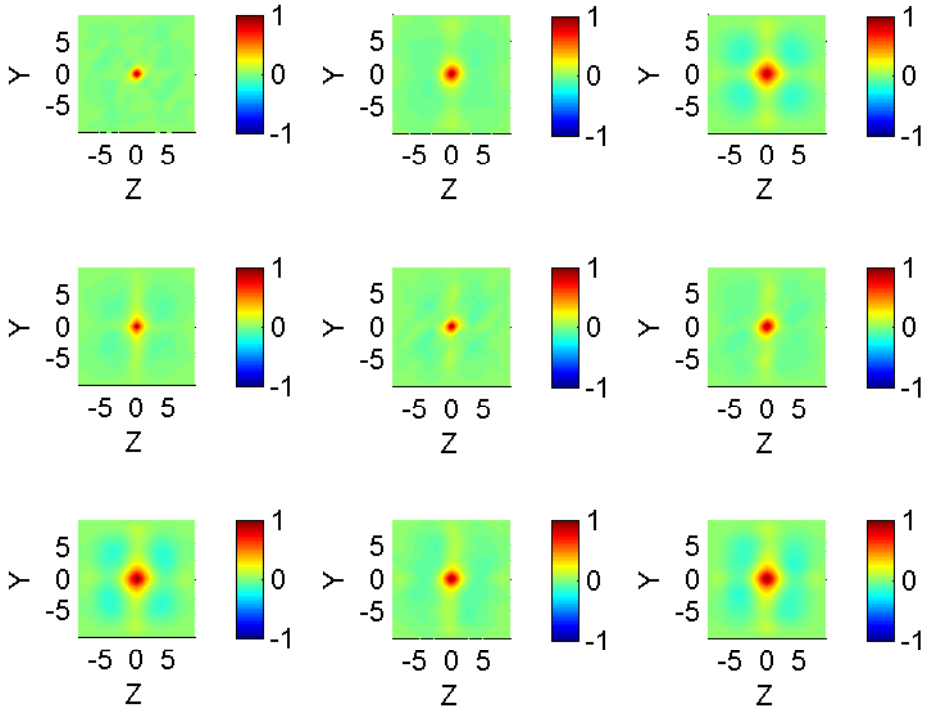


Figure 7.14. Autocorrelation coefficients of $u'$ for the vorticity-forced low heat release case ($M = 4$).

#### 7.3.1.4 CASE IV: Non-Reactive Case

As can be seen in Fig. 7.15, for the nonreactive case, the autocorrelation structures do not change their shape, remaining roughly circular even after passing through the shock location. The correlations grow in size due to the increased disturbance from the shock interaction but shrink further downstream as the turbulence decays. Obviously, without chemical reactions and the introduction of transverse waves, the autocorrelation does not distort to a diamond shape.

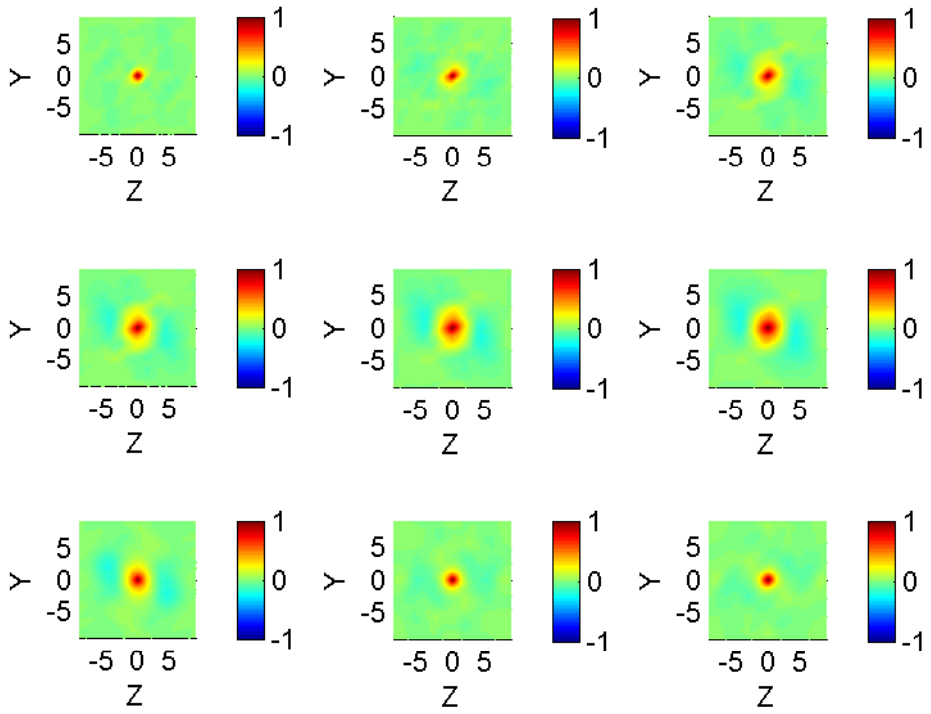


Figure 7.15. Autocorrelation coefficients of $u'$ for the nonreactive case ($M = 4$).

### 7.3.2 High Heat Release Case

#### 7.3.2.1 CASE V: Non-Forced High Heat Release Case

Figure 7.16 shows the autocorrelation coefficients for this case. Since the preshock environment has no turbulence, the autocorrelation coefficient should theoretically be a delta function. It is shown here as a small dot. However, due to the high heat release, the diamond shape is more evident when compared with the similar low heat release case (Fig. 7.12). The autocorrelation remains substantial even at the exit of the computational domain indicating that the disturbances remain strong.

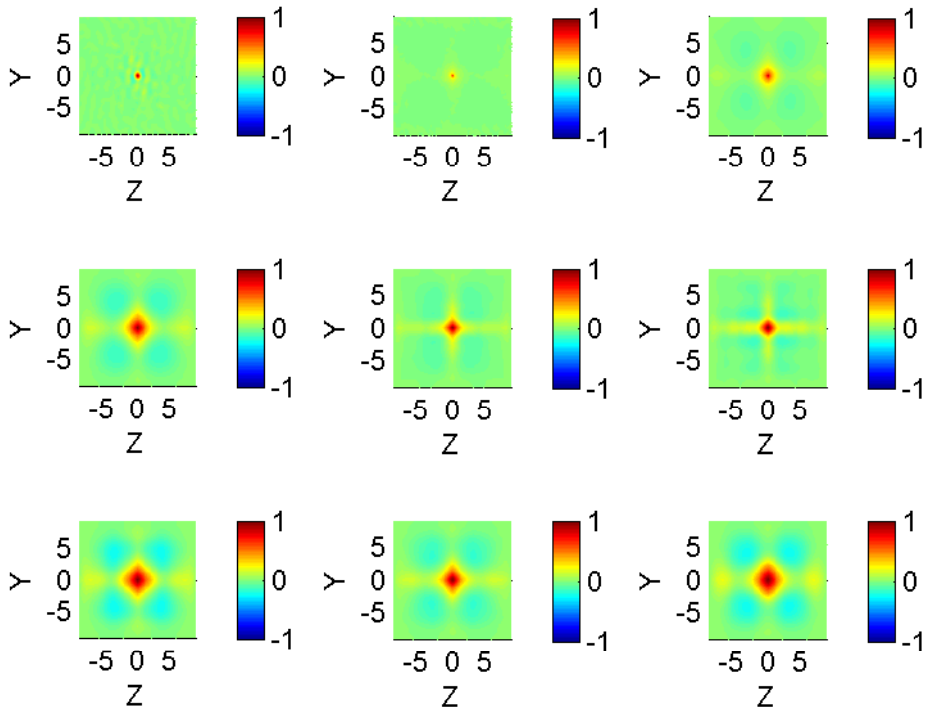


Figure 7.16. Autocorrelation coefficients of $u'$ for the nonforced high heat release case ($M = 5.5$).

#### 7.3.2.2 CASE VI: Entropy-Forced High Heat Release Case

From Fig. 7.16, the autocorrelation structure is similar to that of the low heat release case. The circular shape indicates that the incoming entropic disturbances are sufficiently strong to mask the effects of the transverse waves.

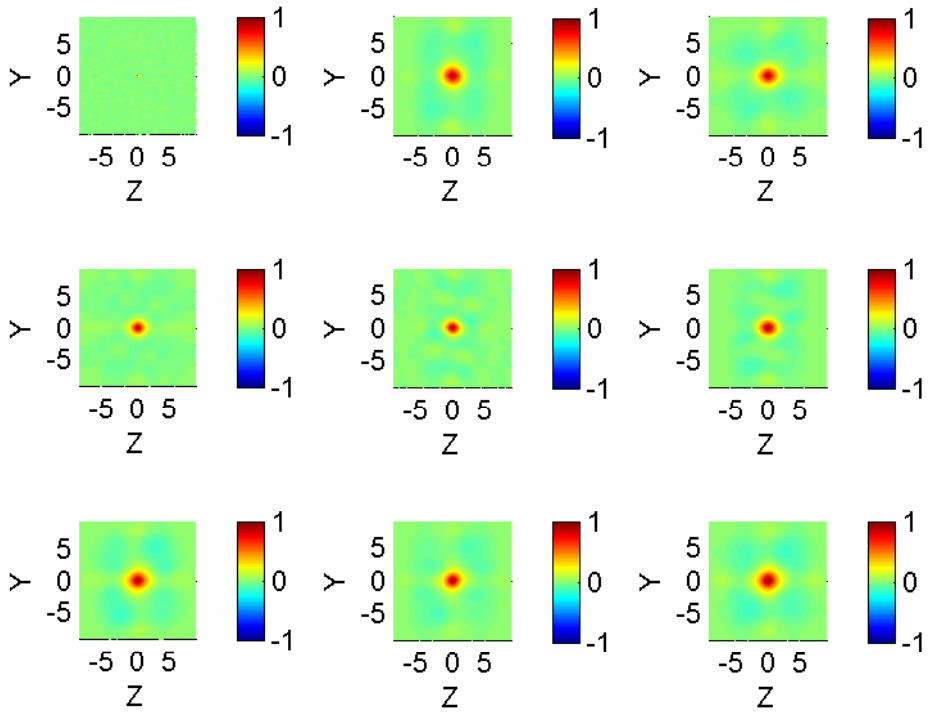


Figure 7.17. Autocorrelation coefficients of $u'$ for the entropy-forced high heat release case ($M = 5.5$).

#### 7.3.2.3 CASE VII: Vorticity-Forced High Heat Release Case

In this case, Fig. 7.18 shows that the correlations start from a circular shape before the shock but change to a diamond shape. The vorticity disturbances are weaker than the entropic ones. Therefore, the correlations of the transverse waves are sufficient to distort the shape to a diamond one.

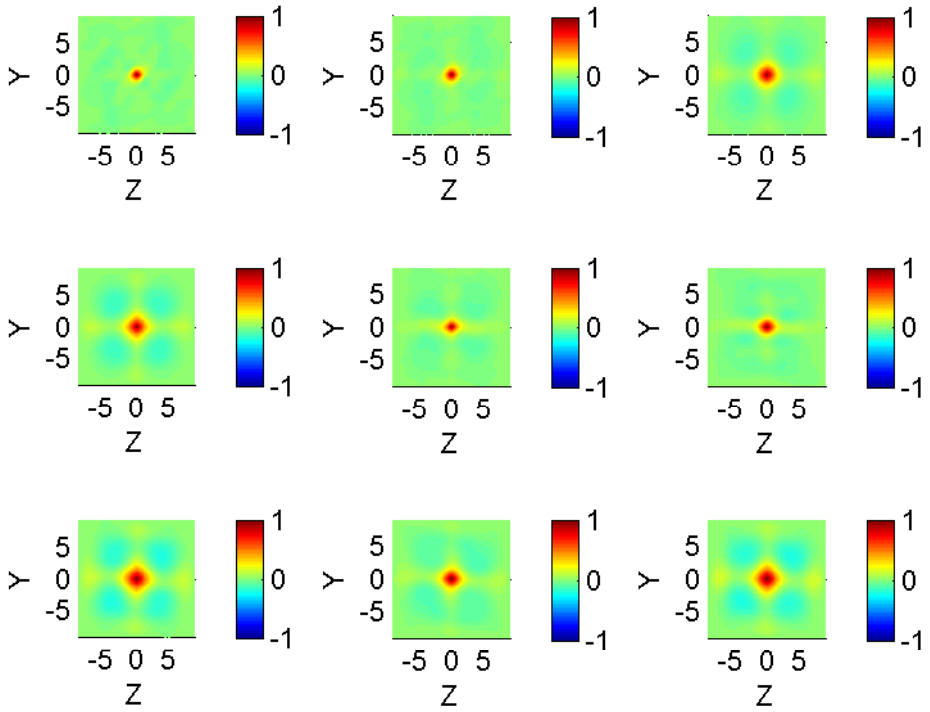


Figure 7.18. Autocorrelation coefficients of $u'$ for the vorticity-forced high heat release case ($M = 5.5$).

# CHAPTER 8

# TACC VISUALIZATION

Resources from the Texas Advanced Computing Center (TACC) were used for the computations whose results are discussed here. TACC resources were also used for visualizing the data. Energy dissipation and vorticity are two important descriptors of small-scale motion which represents the intensity of straining and rotation. Therefore, there behavior is important in both fundamental studies of turbulence as well as in the modeling of combustion or dispersion problems. Enstrophy $\mathcal{E}$ is defined as the integral of the vorticity $\omega(x,t)$ squared given a velocity field as,

$$\mathcal{E} = \omega^2 \tag{8.1}$$

where $\vec{\omega} = \nabla \times \vec{u}$ is the vorticity. Enstrophy can provide insight into vortex stretching, which is an important process in turbulent flows. Vortex stretching is given by $\vec{\omega} \cdot \nabla \vec{u}$ and is strictly a three-dimensional phenomenon. For two-dimensional flow, there is no vortex stretching term and the one non-zero component of vorticity evolves as a conserved scalar. Because of the absence of vortex stretching, two-dimensional turbulence is qualitatively different from the three-dimensional turbulence. Three-dimensional enstrophy is plotted by using the TACC visualization package "VisIT" and support team (led by Mr. Makoto Sadahiro). Visualizations are made in tetrahedrized volume rendering of the iso-surface values of the enstrophy with the onion-peeling option as shown in the below figures.

The above figures (8.1, 8.3) shows that regions of intense vorticity (red iso-contours) and energy dissipation (blue/green volume rendering) occur in organized

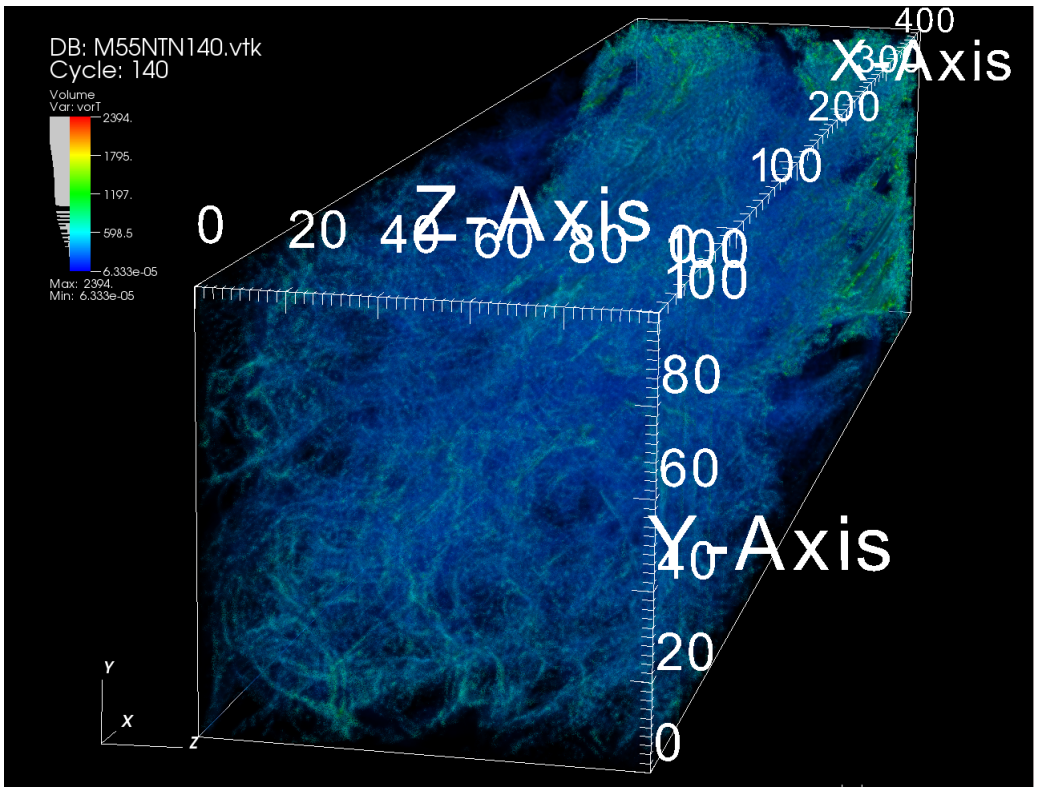


Figure 8.1. TACC visualization showing vortex lines for the vorticity-forced high heat release case.

structures. In particular, large vorticity tends to concentrate in long but thin tubes surrounded by large dissipation.

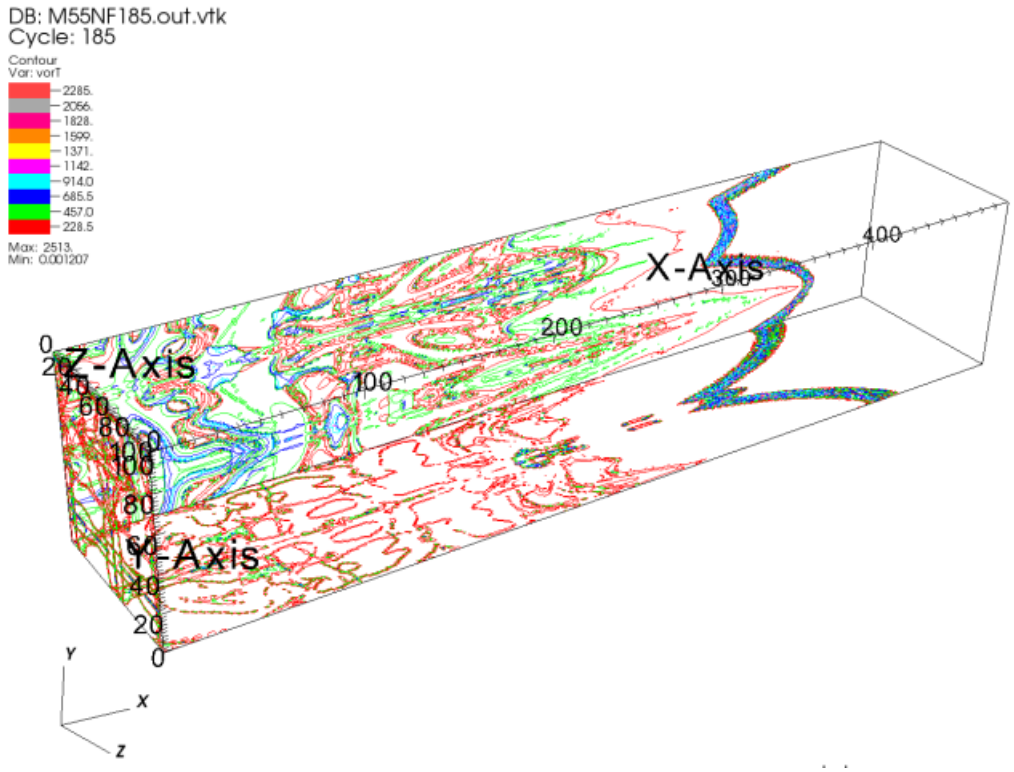


Figure 8.2. Vortical structures changing with movement of flow with respect to shock location for the non - forced high heat release case (Mach number $M = 5.5$).

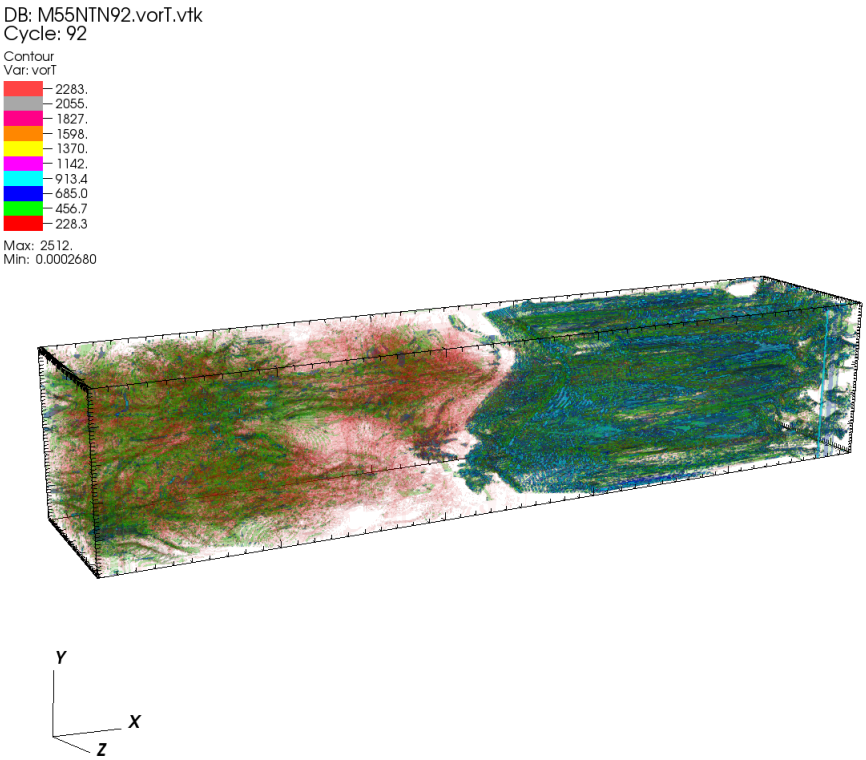


Figure 8.3. Enstrophy for the vorticity-forced high heat release case ($M = 5.5$).

# CHAPTER 9

# CONCLUSIONS AND RECOMMENDATIONS

The present research is a numerical study of the interaction between a detonation wave and compressible, homogeneous, isotropic turbulence. The study is conducted with the detonation wave propagating at either Mach 4 or 5.5, corresponding to low and high heat release respectively. The detonation–turbulence interaction process differs from the non-reactive shock–turbulence analog because of three reasons: exothermicity, the presence of a length scale associated with the detonation structure, presence of natural (intrinsic) fluctuations of the unstable detonation front and the role of induction region in the amplification of convected vortical structures. However, not much work has been done to study the former interaction. Other than the low and high heat release, no initial forcing, entropic forcing and vortical forcing were considered, thereby resulting in six cases. A seventh case is also studied which is of shock–turbulence interaction. The cases were analyzed assuming homogeneity and isotropy in the crosswise planes. At each plane, an ensemble of 100 datasets were averaged to obtain rms velocities and autocorrelation coefficients. For high heat release, entropic perturbations are more effective in reducing the peak intensities compared to vortical perturbations. Entropic forcing increases the probability of high temperature fluid in the reaction zone which causes the formation of hot spot at the higher activation energy compared to the vortical forcing in the same conditions. Significant diamond shape detonation structures are observed in the auto-correlation for the entropic forced cases due to the lateral boundary conditions.

From the velocity variance analysis for the different cases, a different rms distributions are observed. It is also noticed that velocity perturbations reduce the peak intensities but not shifting the peak intensities when comparing the low heat, high heat and non-reactive cases. Longitudinal velocity variances strongly enhanced and then drops back whereas for the transverse velocity variances, it also enhanced. Both longitudinal and transverse velocity variances drop back and return to isotropy. Amplification increases with increasing Mach number for both vortical and entropic fluctuations. Heat release effect (either low or heat heat release) increase the fluctuations in the reaction zone and decrease the intensity in the far-field. Further analysis of the data will be undertaken. These include an examination of the cross-correlations which will provide further statistical understanding of the turbulent field when subjected to straining and heat release. The effect of shock straining and heat release on the evolution of turbulence will require an understanding of the evolution of the enstrophy, the third derivative of the velocity fluctuation and an accounting of the turbulence energy budget. For the last, spectral analysis will be performed. Variation of the non-dimensional parameter $N$ will be helpful in understanding the relative effects of heat release and preshock turbulence on the postshock turbulence. The development of large eddy simulations is also contemplated. Together with realistic chemistry, a computational tool will be available for studying practical problems of interest such as in the development of continuous detonation engines and in blast mitigation, amongst others.

REFERENCES


[1] Y. Andreopoulos, J.H. Agui, and G. Briassulis. Shock Wave &-Turbulence Interactions. *Annual Review Of Fluid Mechanics*, 32(1):309–345, 2000.

[2] J.M. Austin. *The Role of Instability in Gaseous Detonation*. PhD thesis, California Institute of Technology, 2003.

[3] D.S. Balsara and C.W. Shu. Monotonicity preserving weighted essentially non-oscillatory schemes with increasingly high order of accuracy. *Journal of Computational Physics*, 160(2):405–452, 2000.

[4] R. Borges, M. Carmona, B. Costa, and W.S. Don. An improved weighted essentially non-oscillatory scheme for hyperbolic conservation laws. *Journal of Computational Physics*, 227(6):3191–3211, 2008.

[5] F.A. Bykovskii, S.A. Zhdan, and E.F. Vedernikov. Continuous spin detonations. *Journal Of Propulsion And Power*, 22(6):1204–1216, 2006.

[6] G. Ciccarelli and S. Dorofeev. Flame acceleration and transition to detonation in ducts. *Progress in Energy and Combustion Science*, 34(4):499 – 550, 2008.

[7] M. Crespo, S. Jamme, and P. Chassaing. Compressibility effects on the return to isotropy of homogeneous anisotropic turbulence. *EUROMECH European Turbulence Conference*, 2007.

[8] P.A. Davidson. *Turbulence: an introduction for scientists and engineers*. Oxford University Press, USA, 2004.

[9] V. Deledicque and M.V. Papalexandris. Computational study of three-dimensional gaseous detonation structures. *Combustion and Flame*, 144(4):821–837, 2006.

[10] S.B Dorofeev, V.P Sidorov, M.S Kuznetsov, I.D Matsukov, and V.I Alekseev. Effect of scale on the onset of detonations. *Shock Waves*, 10(2):137–149, 2000.

[11] H.S. Dou, H.M. Tsai, B.C. Khoo, and J. Qiu. Simulations of detonation wave propagation in rectangular ducts using a three-dimensional WENO scheme. *Combustion and Flame*, 154(4):644–659, 2008.

[12] F. Ducros, V. Ferrand, F. Nicoud, C. Weber, D. Darracq, C. Gacherieu, and T. Poinsot. Large-eddy simulation of the shock/turbulence interaction. *Journal of Computational Physics*, 152(2):517–549, 1999.

[13] W. Fickett and W.C. Davis. *Detonation: Theory and Experiment*. Dover Pubns, 2001.

[14] V.N Gamezo, D. Desbordes, and E.S Oran. Two-dimensional reactive flow dynamics in cellular detonation waves. *Shock Waves*, 9(1):11–17, 1999.

[15] S.L Gavrilyuk and R. Saurel. Estimation of the turbulent energy production across a shock wave. *Journal of Fluid Mechanics*, 549(-1):131–139, 2006.

[16] B.E Gelfand, S.M Frolov, and M.A Nettleton. Gaseous detonations–A selective review. *Progress In Energy And Combustion Science*, 17(4):327–371, 1991.

[17] I. Glassman and R.A. Yetter. *Combustion*. Academic Pr, 2008.

[18] N.E. Grube, E.M. Taylor, and M.P. Martin. Direct Numerical Simulation of Shock-wave/Isotropic Turbulence Interaction, 2009.

[19] T.L Jackson, M.Y Hussaini, and H.S Ribner. Interaction of turbulence with a detonation wave. *Physics of Fluids A: Fluid Dynamics*, 5:745, 1993.

[20] S. Jamme, J.B. Cazalbou, F. Torrès, and P. Chassaing. Direct numerical simulation of the interaction between a shock wave and various types of isotropic turbulence. *Flow, Turbulence and Combustion*, 68(3):227–268, 2002.

[21] G.S. Jiang and C.W. Shu. Efficient implementation of weighted ENO schemes. *Journal of Comput. Physics*, 126:202–228, 1996.

[22] E. Johnsen, J. Larsson, A.V. Bhagatwala, W.H. Cabot, P. Moin, B.J. Olson, P.S. Rawat, S.K. Shankar, B. Green, HC Yee, et al. Assessment of high-resolution methods for numerical simulations of compressible turbulence with shock waves. *Journal of Computational Physics*, 229(4):1213–1237, 2010.

[23] D.A Kessler, V.N Gamezo, and E.S Oran. Simulations of flame acceleration and deflagration-to-detonation transitions in methane-air systems. *Combustion and Flame*, 157(11):2063–2077, 2010.

[24] A.M. Khokhlov, E.S. Oran, A.Y. Chtchelkanova, and J.C. Wheeler. Interaction of a shock with a sinusoidally perturbed flame. *Combustion and flame*, 117(1-2):99–116, 1999.

[25] J. Larsson and S.K. Lele. Direct numerical simulation of canonical shock/turbulence interaction. *Physics of Fluids*, 21:126101, 2009.

[26] C.K. Law. *Combustion physics*. Cambridge Univ Pr, 2006.

[27] S. Lee, S.K. Lele, and P. Moin. Direct numerical simulation of isotropic turbulence interacting with a weak shock wave. *Journal of Fluid Mechanics*, 251(-1):533–562, 1993.

[28] S. Lee, S.K. Lele, and P. Moin. Interaction of isotropic turbulence with shock waves: effect of shock strength. *Journal of Fluid Mechanics*, 340(-1):225–247, 1997.

[29] S.K. Lele. Compressibility effects on turbulence. *Annual Review Of Fluid Mechanics*, 26(1):211–254, 1994.

[30] A.J Lowe and P.A Davidson. The evolution of freely-decaying, isotropic, two-dimensional turbulence. *European Journal of Mechanics-B/Fluids*, 24(3):314–327, 2005.

[31] K. Mahesh, S.K. Lele, and P. Moin. The influence of entropy fluctuations on the interaction of turbulence with a shock wave. *Journal of Fluid Mechanics*, 334(-1):353–379, 1997.

[32] L. Massa, J.M Austin, and T.L Jackson. Triple-point shear layers in gaseous detonation waves. *Journal of Fluid Mechanics*, 586:205–248, 2007.

[33] L. Massa, M. Chauhan, and F.K Lu. Detonation-turbulence interaction. *Combustion and Flame*, 2011.

[34] L. Massa, M. Chauhan, and F.K Lu. Numerical study of detonation turbulence interaction. *American Institute of Aeronautics and Astronautics*, 2011.

[35] L. Massa and F.K. Lu. The role of the induction zone on the detonation–turbulence linear interaction. *Combustion Theory and Modelling*, 99999(1):1–25, 2011.

[36] H.N. Nagarajan. *Direct Numerical Simulation of Interaction of Detonation Wave with Homogeneous Isotropic Turbulence*. PhD thesis, University Of Texas At Arlington, 2010.

[37] S. Pirozzoli. Conservative hybrid compact-WENO schemes for shock–turbulence interaction. *Journal of Computational Physics*, 178(1):81–117, 2002.

[38] S.B. Pope. *Turbulent Flows*. Cambridge University Press, 2000.

[39] J. Qiu and C.W. Shu. Finite difference WENO schemes with Lax-Wendroff-type time discretizations. *SIAM Journal on Scientific Computing*, 24(6):2185–2200, 2003.

[40] P.S. Rawat and X. Zhong. Numerical Simulation of shock–turbulence Interactions using High-Order Shock-Fitting Algorithms. *American Institute of Aeronautics and Astronautics*, 2010.

[41] Y.X. Ren, M. Liu, and H. Zhang. A characteristic-wise hybrid compact-WENO scheme for solving hyperbolic conservation laws. *Journal of Computational Physics*, 192(2):365–386, 2003.

[42] H.S. Ribner. Spectra of noise and amplified turbulence emanating from shock–turbulence interaction. *AIAA Journal*, 25:436–442, 1987.

[43] R.S. Rogallo. Numerical experiments in homogeneous turbulence. *NASA STI/Recon Technical Report*, 81, 1981.

[44] Y. Shen, G. Zha, and X. Chen. High order conservative differencing for viscous terms and the application to vortex-induced vibration flows. *Journal of Computational Physics*, 228(22):8283–8300, 2009.

[45] J. Shi, C. Hu, and C.W. Shu. A Technique of Treating Negative Weights in WENO Schemes. *Journal of Computational Physics*, 175(1):108–127, 2002.

[46] C.W. Shu. Essentially non-oscillatory and weighted essentially non-oscillatory schemes for hyperbolic conservation laws. *Advanced Numerical Approximation of Nonlinear Hyperbolic Equations*, 1998.

[47] C.W. Shu and S. Osher. Efficient implementation of essentially non-oscillatory shock-capturing schemes. *Journal of Computational Physics*, 77(2):439–471, 1988.

[48] B. Texier and K. Zumbrun. Transition to longitudinal instability of detonation waves is generically associated with Hopf bifurcation to time-periodic galloping solutions. *Arxiv preprint arXiv:0812.3582*, 2008.

[49] S. Xanthos, M. Gong, and Y. Andreopoulos. Velocity and vorticity in weakly compressible isotropic turbulence under longitudinal expansive straining. *Journal of Fluid Mechanics*, 584:301–335, 2007.

## BIOGRAPHICAL STATEMENT

Monika Chauhan was born in New Delhi, India on 13th November 1987. She received her Bachelor of Technology degree in 2008 from Lucknow University, India and fulfilled her wish of becoming a mechanical Engineer. Her Master of Science degree in mechanical engineering from The University of Texas at Arlington in 2011 again fullfilled her wish of attaining a higher degree in advanced technology and engineering.

Her research in the Mechanical and Aerospace Engineering Department, University of Texas at Arlington, is in the area of computational fluid dynamics, turbulence, combustion and aerospace. Her invaluable industrial experience as an engineering intern in Meteodyn America Inc. (a wind energy company, Philadelphia, USA), National Thermal Power Plant (NTPC-India), Larsen and Tubro - Sargent and Lundy Ltd. (India) and Northern Railways (India) gave her outstanding collaborative industry credentials. Her undergraduate final semester project in CATIA V5 R17 between Dassaults Systems (France) and PLMCC (India) to analyzed and designed the chassis and body prototype for the Shell Eco Marathon Car (a fuel efficient car) was the most challenging and inevitable part of her undergraduate experience.

She is a student member of AWEA (American Wind Energy Association), AIAA (American Institute of Aeronautics and Astronautics), ASME (American Society of Mechanical Engineers), NSBE (National Society of Black Engineers), SWE (Society of Women Engineers) and WoWE (Women of Wind Energy).

This paper documents the independent research that she has done in attaining the Master of Science in Mechanical Engineering.